DISCLAIMER

ORNL/TM-2025/4057

Completion of Transport Property Measurements on Multiple Actinide Fluoride Mixtures

Nicholas Termini*
Ryan Chesser*
Bruce McNamara†
Amanda Leong‡
Jaewoo Park‡
Jinsuo Zhang‡
Will Tomeo§
Andy Anderson*
Anthony Birri*

September 2025

*Oak Ridge National Laboratory, Oak Ridge, TN
†Pacific Northwest National Laboratory, Richland, WA
‡ Virginia Polytechnic Institute and State University, Blacksburg, VA
§ University of Michigan, Ann Arbor, MI

OAK RIDGE National Laboratory

ORNL IS MANAGED BY UT-BATTELLE LLC FOR THE US DEPARTMENT OF ENERGY

ORNL/TM-2025/4057

Nuclear Energy and Fuel Cycle Division

Completion of Transport Property Measurements on Multiple Actinide Fluoride Mixtures

Nicholas Termini*
Ryan Chesser*
Bruce McNamara†
Amanda Leong‡
Jaewoo Park‡
Jinsuo Zhang‡
Will Tomeo§
Andy Anderson*
Anthony Birri*

Report on the completion of the following milestone:
Milestone M2AT-25OR0705041
September 2025

*Oak Ridge National Laboratory, Oak Ridge, TN
†Pacific Northwest National Laboratory, Richland, WA
‡ Virginia Polytechnic Institute and State University, Blacksburg, VA
§ University of Michigan, Ann Arbor, MI

Prepared by
OAK RIDGE NATIONAL LABORATORY
Oak Ridge, TN 37831
managed by
UT-Battelle LLC
for the
US DEPARTMENT OF ENERGY
under contract DE-AC05-00OR22725

CONTENTS

LIST OF FIGURES

ACKNOWLEDGMENTS

This work is funded by the US Department of Energy's Office of Nuclear Energy Molten Salt Reactor Campaign under the Advanced Reactor Technology program. The authors would like to thank Joanna Mcfarlane and Kevin Robb at Oak Ridge National Laboratory for their insights and expertise regarding molten salt chemistry, handling, and experimental considerations. The viscosity measurements made in this work could not have been performed without the careful and precise welding performed by the Materials Engineering and Testing Corporation. The authors would like to thank Bob Sitterson, Craig Gray, and David Bryant at Oak Ridge National Laboratory for assisting in property measurement system modifications throughout the fiscal year.

ABBREVIATIONS

CSV	comma-separated value
DOE-NE	Department of Energy Office of Nuclear Energy
GUI	graphical user interface
ICP-MS	inductively coupled plasma mass spectrometry
MSR	molten salt reactor
MSTDB-TP	Molten Salt Thermal Properties Database—thermophysical
NEAMS	Nuclear Energy Advanced Modeling and Simulation
ORNL	Oak Ridge National Laboratory
RK	Redlich-Kister
PNNL	Pacific Northwest National Laboratory
SS-316	stainless steel 316
VT	Virginia Tech
XRD	x-ray diffraction

SUMMARY

One of the missions of the US Department of Energy's Office of Nuclear Energy (DOE-NE) Molten Salt Reactor (MSR) Campaign under the Advanced Reactor Technology program has been to experimentally measure thermophysical properties of MSR-relevent salt systems, with the intent of supporting the development of the Molten Salt Thermal Properties Database (MSTDB). This database is jointly funded by the DOE-NE Nuclear Energy Advanced Modeling and Simulation Program and the MSR Campaign. Multiple DOE national laboratories, including Oak Ridge National Laboratory (ORNL), have been conducting measurements of thermophysical properties to support MSTDB development and provide MSR developers with access to new data that has been measured using modern methodologies and more advanced sample characterization techniques. These data may either fill gaps in the database or provide updated higher quality data to replace legacy data.

Researchers at ORNL have recognized significant gaps in the transport property data of actinide-bearing fluoride salt systems of MSR industry interest. Moreover, for the data present in MSTDB in this category, the uncertainty margins are generally high, leading to questionability in our current understanding of the thermophysical characterization of actinide fluoride mixtures. As such, the focus of this study has been to generate new transport property data of actinide fluoride mixtures that are of immediate interest to MSR developers. Specifically, the mixtures NaF-UF_4 (78 - 22 mol%) and NaF-KF-UF_4 (57-16.04-26.91 mol%) have been studied—NaF-UF_4 for thermal conductivity and viscosity and NaF-KF-UF_4 for viscosity. Thermal conductivity measurements have been conducted with a variable gap apparatus, whereas viscosity has been measured with a rolling ball viscometer. Methodological and calibration details are provided for both measurement processes, along with measurement system updates that have enabled easier manufacturing of components and fewer challenges associated with conducting the measurements themselves. The resultant data collected for NaF-UF_4 (78–22 mol%) and NaF-KF-UF_4 (57-16.04-26.91 mol%) have been compared with relevant mixture data within the thermophysical arm of the MSTDB (MSTDB-TP).

1. INTRODUCTION

Molten salt reactors (MSRs) can only be designed, modeled, licensed, and operated assuming that the thermophysical properties of the coolant and fueled salts are well-characterized. These thermophysical properties are inputs to models that can predict the steady-state temperature distribution, transient thermal response, heat flow and dissipation in accident scenarios, and thermal hydraulic feedback for neutronic performance. In support of the developing MSR industry, multiple national laboratories have endevoured to measure thermophysical properties of key molten salt mixtures [1–9]. This effort is funded by the MSR Program under the US Department of Energy Office of Nuclear Energy (DOE-NE). This is a crucial time to provide such data publicly because three domestic test MSRs are planned to come online within the decade [10–12]. These test MSRs, which represent a stepping stone to deployment of commercial-scale MSRs, are being developed by several entities [10, 13–15]. The primary thermophysical properties of interest are density, viscosity (kinematic), thermal conductivity, and heat capacity. Surface tension and optical properties also play key roles in thermal hydraulic performance. Surface tension captures the interplay of cohesive forces (within the molten salt) with adhesive forces (between the liquid and its container), has major implications to multiphase flow such as bubble/droplet formation and behavior, and affects other properties such as volatility and boiling temperature [16, 17].

Available data on thermal conductivity and viscosity are particularly sparse [18], and several instances of significant discrepancies exist among duplicate experimental studies [19, 20]. When thermal conductivity is measured directly, steady-state heat flux is applied across a molten specimen to measure a temperature difference, and other modes of heat transfer besides conductive heat flow across the sample must be exhaustively accounted for, which can be difficult. These challenges are evidenced by the widespread data for steady-state techniques applied to eutectic LiF–NaF–KF (FLiNaK) [21], for example. Transient techniques (e.g., laser flash analysis [22]) for measurement have similar concerns and are also indirect measurements in that they measure thermal diffusivity and rely on other properties (e.g., heat capacity and density) to calculate thermal conductivity inheriting their uncertainty. Whether viscosity is measured with an oscillational [23], rotational [24], or gravitational [25] technique, the measurements can be particularly sensitive to bubbles, sample inhomogeneity, temperature, corrosion of the measurement device, and particulate sample impurities. Despite these challenges, the need to obtain accurate measurements for a variety of potentially corrosive, hygroscopic salt mixtures (e.g., UCl_3 bearing melts) persists, given the key data gaps of relevant salt mixtures for the developing MSR industry. As such, Oak Ridge National Laboratory (ORNL) is focused on developing thermal conductivity and viscosity systems that (1) can handle such mixtures; (2) have a low, well-characterized uncertainty; and (3) more recently, can be used for actinide-bearing mixtures [1, 25–31].

The main driver behind the selection of molten salt mixtures is the thermophysical arm of the Molten Salt Thermal Properties Database (MSTDB-TP) [32], which is funded by the Nuclear Energy Advanced Modeling and Simulation (NEAMS) program under DOE-NE. The database has been largely informed by a road map for thermal property measurements put forth in 2021 [33]. The road map defines the key pseudo-binary systems to be characterized to fully understand thermophysical properties for all higher-order mixtures that the industry may consider for coolant and fueled salts. Exhaustive data collection has shown general trends for viscosity and thermal conductivity of actinide-bearing multicomponent fluoride systems, but the existence of large discrepancies and the general sparseness of data provide motivation to perform additional measurements of actinide fluoride systems. Regarding viscosity, the current understanding of actinide-bearing fluoride systems is limited to a small group of studies performed at ORNL or by collaborating institutions in the 1950s and 1960s [34–38]. Only a

handful of studies have looked at thermal conductivity higher-order fluoride actinide systems [39–42].

Efforts in FY 2024 [31] focused on actinide-bearing chloride mixtures, whereas efforts in FY 2025 serve as an extension of that effort, with a focus on the measurement of actinide-bearing, multicomponent fluoride salt systems for both viscosity and thermal conductivity. The goal was to investigate the effects of the addition of actinide fluorides (specifically UF_4) in mixtures because actinides are predicted to have substantial impacts on both transport properties. Results from the experimental measurements described herein can be compared with kinetic theory models for thermal conductivity and Redlich-Kister (RK) models for viscosity; these models have been developed tangentially through efforts on the MSTDB-TP [43]. Other efforts this year fall under experimental optimization. The goals of these efforts were to address major time sinks encountered in fabrication/measurement processes and to improve the characterization of uncertainty of the measurements. As such, this report describes a simplification and redesign of manufactured components to address sources of systematic experimental error and streamline the ordering to measurement process. Finally, data analysis graphical user interfaces (GUIs) have been implemented for better processing and visualization of data.

2. EXPERIMENTAL METHODS

2.1 ROLLING-BALL VISCOMETER

2.1.1 System Overview and Working Principles

The rolling ball viscometer operates on the principle of measuring the terminal velocity of a ball rolling through a tubular crucible at or near terminal velocity. The viscosity, μ, is isolated by balancing the forces along the axis on which the ball is traveling. Namely, an opposing viscous force, a buoyancy force, and a gravitational driving force are all acting on the ball in this axis. After defining the force contribution equation involving all of these forces along this axis, it can be shown that μ is described by

$$\mu = \frac{K(\rho_b - \rho_f)t\sin(\theta)}{L}, \tag{1}$$

where K is a calibration constant, ρ_b is the density of the ball, ρ_f is the density of the fluid (in this case molten salt), t is the time the ball takes to roll some length L, and θ is the crucible's angle of inclination. The calibration factor K is important because it accounts for nonanalytical factors (e.g., mainly friction and drag), and K is determined through careful calibration efforts described in the next section. Friction is assumed to be consistent through both calibration and experiment, which leaves the selection of K for an experiment dependent on flow characteristics. The flow characteristics that have the largest effect on the experiment are wall effects and drag, which are matched by the diameter ratio of the ball and the wall and the Reynolds number, respectively. This means that if a salt measurement has the same diameter ratio and Reynolds number as that of a calibration experiment, the K determined via calibration is deemed valid for the salt measurement. Therefore, the calibration process involves careful planning for mapping potential diameter ratios and Reynolds numbers expected for a given salt experiment.

A general depiction of the crucibles used to enable rolling ball terminal velocity measurements in this study is shown in Figure 1. All crucible designs have two sections: a larger-diameter loading section (depicted by the top image) where the ball has a place to rest after insertion into the crucible, and a smaller-diameter measurement section in which the measurement takes place via tracking of the ball's

velocity. Having a loading section allows the ball to come to temperature within the salt to ensure no initial salt–ball interaction interferes with the measurement and also to minimize entry uncertainty within the measurement section. Several crucible designs have been implemented to address the variety of challenges and compatibility considerations associated with molten salts. A bare glass (fused silica) crucible can be used for non-actinide–bearing chlorides, with the advantage being that the ball can be viewed and tracked optically. The crucibles are inexpensive to fabricate; allow for fast and simple measurements and for clear identification of problems (such as bubble formation) within the measurement section; and are highly inert to the chloride salts. The drawbacks with glass are that (1) fluoride salts cannot be measured due to fluoride etching of glass and (2) the fragility of glass crucibles makes their use too much of a safety hazard with actinides as the primary material boundary from the outside environment. Another disadvantage of glass is the material mismatch between the stainless steel 316 (SS-316) ball and the glass crucible that results in a thermal expansion mismatch requiring careful mapping of the diameter ratio, depending on temperature in calibration. Glass crucibles have not been used in experiments reported herein, but additional details regarding glass crucibles can be found in Birri et al. [25]. Steel crucibles, however, can be used to safely measure both actinide chloride and fluoride salts, but they do not offer the major advantage of easy viewing, instead requiring x-ray imaging to track the ball. However, the same material can be used for the ball and crucible, removing the uncertainty of a thermal expansion mismatch.

With the major issues being reported associated with the steel crucible designs used in the previous FY [31], a redesign of the SS-316 crucible was implemented. The new design has a measurement section with the axis of rotation at its axial center, while maintaining the separate loading and measurement sections with a ledge for the ball to come to a stop for thermal equilibration before crucible rotation, as shown in Figure 2. This ledge is achieved by inserting a smaller slip pipe with the appropriate inner diameter and wall thickness for x-ray measurement into a larger pipe that matches the outer diameter of the loading section. The measurement section and the loading section pipes are partially cut in half across their radial axis and weld-sealed together to form this junction. The crucible can then be rotated to allow the ball to fall into the slip pipe measurement section. This design has many advantages such as being centerline with the axis of rotation, thereby reducing the effects of axial rotation on the measurement. The design is also easier to manufacture, requiring no specialty parts and less specialized welding and cutting.

A secondary containment has been also designed to fit around a glass crucible for a salt experiment. For actinide chloride measurements, this allows for the benefit of the inert glass interface while removing the risk of actinide release if the glass crucible breaks. X-ray imaging is required to track the ball progress with the steel secondary containment. Pictures of all the designs are shown in Figure 3.

An overall view of the viscosity system with its more recent updates is shown in Figure 4. The furnace is a Thermcraft XST-4-0-12-1 that was modified to increase the distance between both furnace halves to allow for (1) viewing of the glass crucible through a small viewing window and (2) x-ray penetration without significant attenuation for imaging. The rotational stage connects to the crucible, which is inserted into the furnace and allows for automated rotation through communication with the power supply. A custom Python script was written to communicate with the power supply API and rotate the crucible to the exact angle to allow the ball to enter the crucible but not over rotate, so that the crucible is still rotating during the measurement. A piping network is connected to the crucible to allow for vacuum and inert gas back filling. In addition, a ventilation stack—into which the vacuum exhausts gas from the piping network—allows for measurement of actinide salts that may produce radioactive gases from their inherent vapor pressures or a small amount of HCl or HF through hydrolysis upon melting. A large, vacuum-rated tank is connected to the control volume of the crucible during testing to ensure minimal pressure buildup in the crucible during

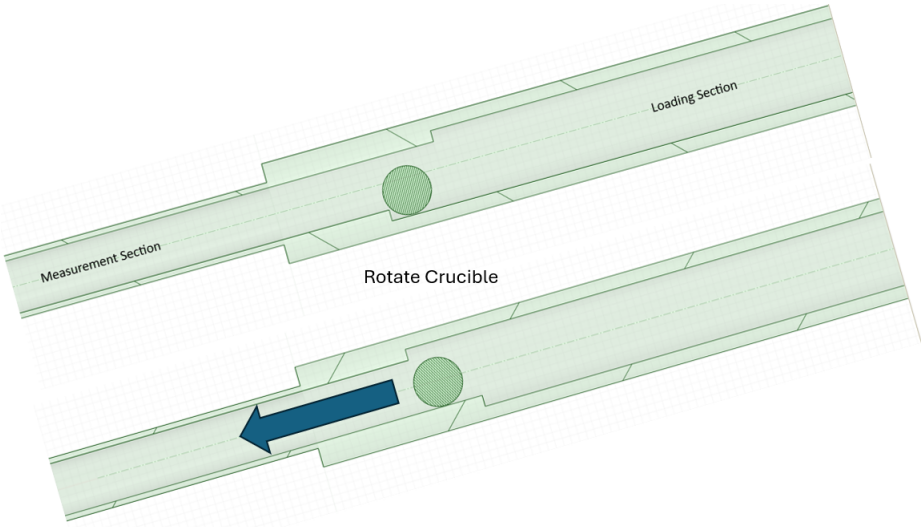

Figure 1. Depiction of the crucibles used to measure viscosity in this study (adopted from [1]). The upper image shows a crucible in the initial orientation when staging a measurement, and the lower image shows a crucible after rotation during measurement.

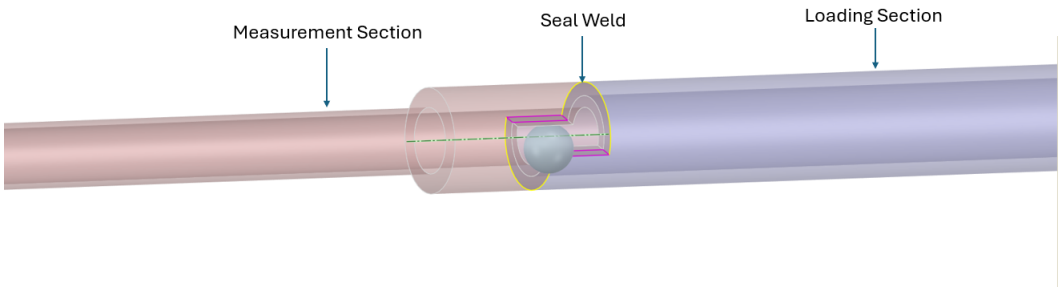

Figure 2. A 3D transparent rendering of the new SS-316 crucible design. The pink portion is the measurement section, and the blue area is the loading section, which is affixed to the rotating stage.

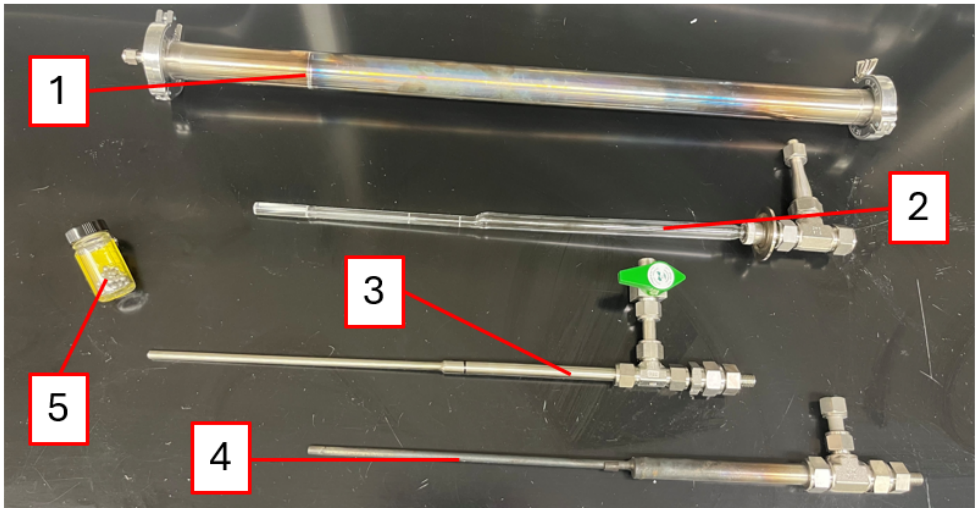

Figure 3. Photograph of the glass and stainless steel crucibles used in this study: (1) the outer containment for glass crucibles to enable actinide chloride measurements, (2) a glass crucible, (3) a new SS-316 crucible, (4) a used SS-316 crucible based on the old design from [31], and (5) SS-316 balls used for measurements.

the heating process in measurements. The Golden Engineering XRS4T x-ray–generating device used for measurements emitted single pulses to capture images of the ball rolling through the crucible during either calibration or salt measurements.

A few components added to the system are not shown in Figure 4. A Ultra-high purity (99.999%) Ar gas tank supplied the control volume of the system, which then fed through an additional in-line gas purifier (Agilent BOT-4) to trap potential oxygen in the feed gas. The x-ray imaging panel is a Varex Imaging x-ray diffraction (XRD) 3025 with a $3,008 \times 2,512$ pixel matrix (100 μm pixel pitch). Commercial software for this device is coupled with a Raspberry Pi microcontroller to coordinate the firing of the XRS4T to the image capture window of the XRD 3025. The x-ray pulses are 10 ns long. Finally, pneumatic arms were added to the test stand to hold the furnace at a particular angle, allowing for precise setting of the furnace angle as measured with the Wixley WR365 Digital Angle Gauge.

2.1.2 Crucible Calibration

Each crucible is calibrated using a variety of National Institute of Standards and Technology standardized viscosity oils. The overall purpose of the calibration process is to account for experimental factors inherent to the crucible itself (e.g., wall effects) and for fluid flow forces consistent from calibration to experiment (e.g., flow regime effects), which presents as a calibration factor K. The Reynolds number (Re) and the ball diameter–to–crucible diameter ratio (d/D) have been determined to have the largest effects on K, and K is assumed to be the same for each scenario where both Re and d/D are identical (or matched through interpolation).

Although the principle behind calibration is the same, each crucible type has a different approach to the calibration process because of material differences during the actual salt experiment. For glass, multiple ball sizes must be considered because of the mismatch in the expansion between the stainless steel ball and

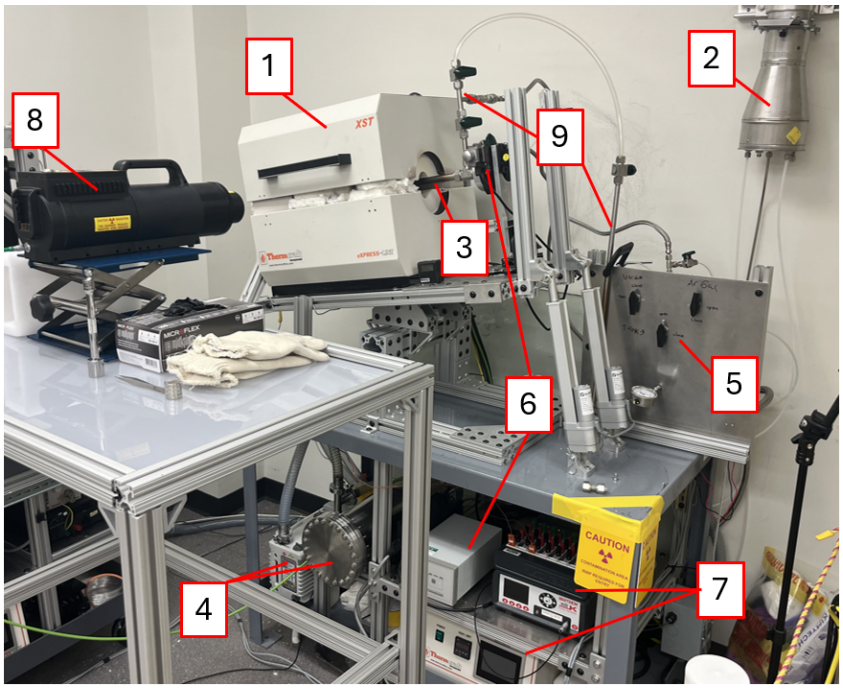

Figure 4. Photograph of the most recent iteration of the rolling ball viscometer used in this study, with most components shown: (1) furnace, (2) ventilation stack, (3) crucible, (4) backfill and pressure maintenance system, (5) gas control, (6) rotation control, (7) heating and temperature control, (8) x-ray generating device, and (9) ball entry system.

the glass at high temperatures, resulting in a new d/D ratio for each temperature measured. The ball diameters chosen for calibration are not meant to exactly match the expected d/D ratio during a measurement. Rather, the diameters should cover a range of d/D ratios that can be interpolated to match the experimental $(d/D)_m$. With enough calibration measurements, a contour can be produced for each calibrated crucible, as shown in Figure 5.

For steel, the process is simpler: only one ball size is needed because the ball and the crucible are both SS-316 and should expand at the same rate. Both crucible types are measured in N4, N2, and N1 oils (Viscosity Standards by Cannon) at different angles to cover a range of *Re* expected in the salt, as shown in Figure 6.

Glass crucibles are measured visually. The terminal velocities are measured by finding the time a ball takes to pass a marked test section on the glass. The time is initially taken manually in the lab and is confirmed by analyzing a video taken of each trial. For the calibration process, an automated measurement device was designed to take time measurements using a system of photointerrupters. This device is explained in more detail in Section 4.1.

Steel crucibles, on the other hand, are measured using an x-ray imaging system, as discussed in Section 2.1.1. Steel weld pins were affixed to a catch tray below the crucible at a fixed distance in the same axis as that of the measurement section for a consistent scale for the image. The x-ray generator is connected to a circuit that can be programmed to trigger consistently at a set time. Each ball position is represented by a single image, in which the ball pixel position can be identified. Using the weld pins to create a pixel length scale, the ball's position can be plotted over time, and velocity can be determined.

2.1.3 Salt Measurement Process

The first step in any salt measurement procedure is thorough cleaning of all equipment. Glass crucibles for chloride salt measurements are rinsed thoroughly, filled with water, and placed in an ultrasonic bath for 1 h. This process is then repeated with ethanol. Next, the crucible is vacuum dried at 300°C. For stainless steel crucibles, ball bearings, and the steel valve attachment for both crucibles, the same procedure is used, but an additional bath cycle is performed with acetone. This step is not performed with glass to avoid etching. The steel ball bearings are then vacuum dried at 300°C in a sealed container for a minimum of 3 h. Next, the containers are backfilled with ultra-high purity (99.999%) Ar passed through the BOT-4 traps and sealed for the experiment. Once the crucibles are thoroughly dried, they are transferred to an inert glove box for salt loading.

Typically, as-received salts (e.g., alkali chloride salts from commercial manufacturers) are placed in a vacuum furnace and heated to 200°C to drive off any oxygen or moisture contamination before weighing. The dried component salts are then weighed to the desired composition for the experiment. The salt mass is chosen to provide sufficient volume for filling the measurement section and 1–2 cm of the loading section. This allows the ball bearing to be submerged in the salt and equilibrated to the salt temperature before being transferred to the measurement section when a test is performed. Salts are mixed thoroughly and transferred to an inert Ar glove box for loading into the crucible. Once the crucible is loaded, the valve is attached to seal the crucible with an inert atmosphere. The crucible is removed from the glove box and transferred to the furnace, and the Ar supply is attached to the other side of the valve. This supply line is purged and refilled several times with Ar to remove oxygen and moisture before the valve is opened and the contents of the crucible are exposed.

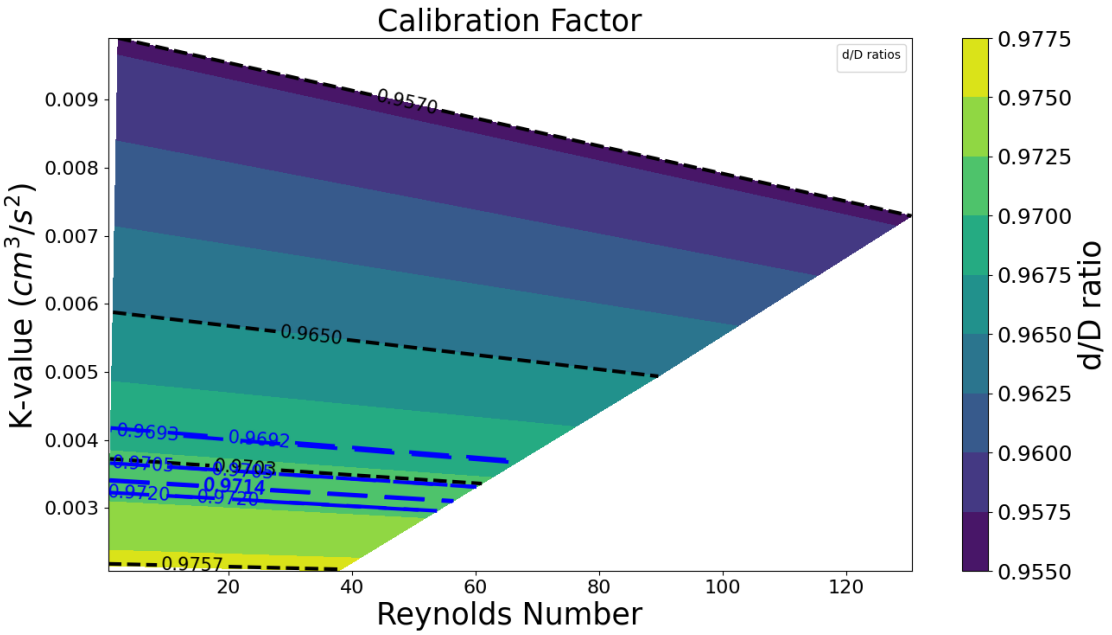

Figure 5. Calibration factor (K) as a function of Reynolds number for a glass crucible fitted to different d/D ratios (dotted black lines) at different experimental temperatures (dashed blue lines) for NaCl-KCl (50-50 mol%).

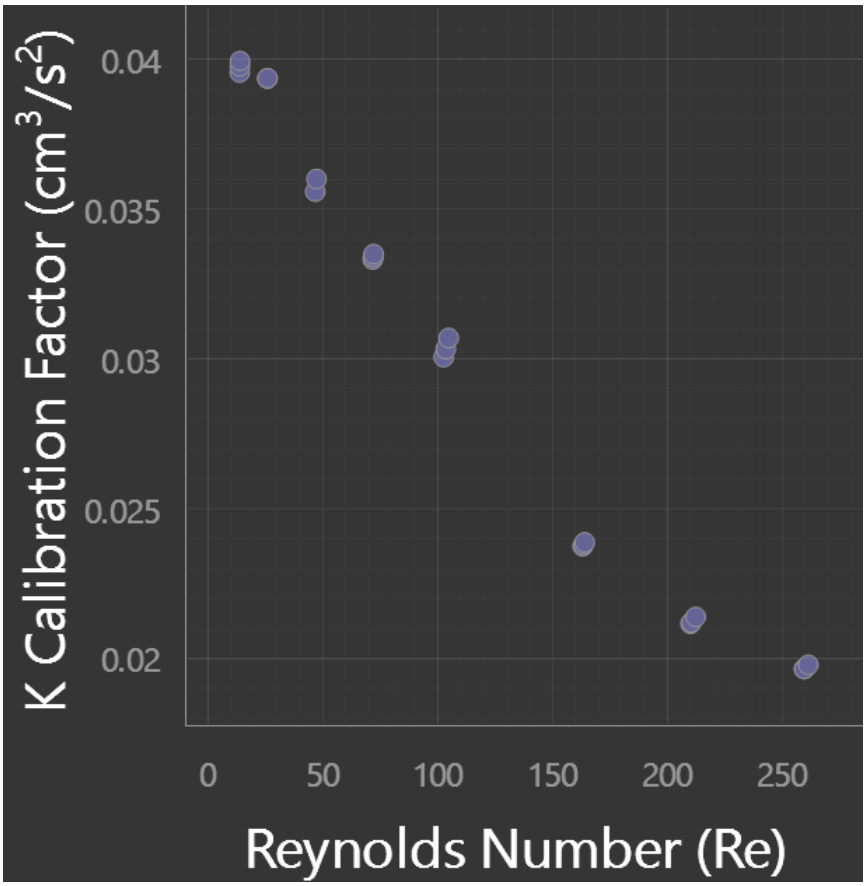

Figure 6. Calibration factor (K) as a function of Reynolds number for a stainless steel crucible.

To perform a measurement, each ball needs to be loaded into the crucible. An inert container of clean, dried ball bearings is connected to the top of the valve structure. The transfer line is cleared and refilled to ensure inert atmosphere. One ball bearing is carefully transferred from the container to the valve structure, where it is dropped into the loading section. The ball bearing rolls into the loading section of the crucible and is submerged into the molten salt. This process often entrains some small gas bubbles onto the ball within the loading section, and it also freezes a layer of salt around the room-temperature ball. A few minutes are given for the ball to equilibrate to the salt temperature and remelt the frozen salt layer. Then the crucible is again agitated to drive off any gas bubbles attached to the ball's surface.

To perform the test, the crucible is rotated to allow the ball to roll into the measurement section. In the glass crucible, the measurement section has white etch marks spaced 5 cm apart. The rolling ball is filmed during transfer to the measurement section until the ball reaches the end of the crucible. In post-experiment analysis, the etch marks provide a reference length scale, and the video frame time stamps provide the reference time scale. These references allow the rolling ball's terminal velocity to be determined. The x-ray system is activated before the ball's transfer into the measurement section. X-ray images are taken at desired time intervals based on triggering with a microcontroller and continue to be taken until the ball reaches the end of the crucible. The weld pin reference length is adjusted for thermal expansion based on temperature measured.

Three identical balls (±0.0005") are tested at each temperature, started with the highest temperature at which data are intended to be collected. The temperature setting is then lowered to the next chosen temperature. Approximately 1 h is given to allow the system to equilibrate at the new temperature. Once the experiment is complete, the furnace temperature is ramped down to room temperature, and the videos or x-ray images are saved for post-experiment analysis. Once the crucible is cooled, it is removed from the furnace and stored safely for disposal. A small sample of the frozen salt is typically removed for further analysis to determine its exact composition and to identify any contamination; post-analysis results are not included in this report but will be documented in follow-on publications regarding the measurements conducted in this report. Data on the resulting terminal velocities, along with consideration of the thermal expansion effect on d/D ratio, are used to calculate the viscosity of the molten salt (discussed in more detail in the previous section). An Arrhenius expression is fitted to the experimental data to provide the correlation with temperature.

A systematic investigation of experimental uncertainty was performed via Gaussian error propagation to identify sources of uncertainty and to quantify their effects on viscosity results. The uncertainty sources identified include length of measurement section, inclination angle of the rolling ball, measurement time, fluid density, ball density, and temperature. Figure 7 compares the contribution of each source to uncertainty in the viscosity measurement result. Based on these contributions, the uncertainties in these measurements have shown a general tendency to be ≈10%, at least for glass crucible measurements, assuming an absence of additional confounding factors (e.g., bubble impacts, extreme surface roughness, or impurity suspension effects). More detail on the uncertainty propagation mathematics utilized herein can be found in Birri et al. [25], in which a detailed account is provided on each of the variables which impact the working equations used to calculate viscosity, the justifications for the decisions regarding their uncertainties, and the manner by which error propagation is carried out.

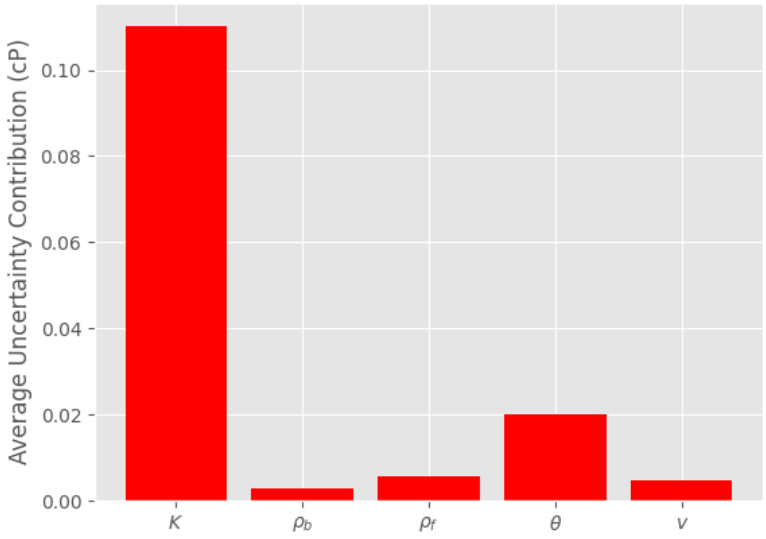

Figure 7. Assessed contributions of uncertainty to the viscosity result during the measurement of LiCl in a steel crucible, where K is the calibration factor, ρ_b is the density of the ball, ρ_f is the density of the fluid, v is the terminal velocity, and θ is the angle of inclination.

2.1.4 Benchmarking Newly Designed Crucible with LiCl

To ensure that the new design is sufficient for viscosity measurements, pure LiCl (Sigma Aldrich, 99.95% trace metal basis) was measured at three temperatures (928, 976, and 1,030 K) using the new SS-316 design. The salt was predried in a vacuum furnace, measured, and loaded into a crucible. The loaded crucible was then dried under Ar cover gas for 3 h before being ramped up to fusing temperature (1,030 K), where it was held for 24 h before measurements began.

The experimental results (Figure 8) show close agreement with the recommended MSTDB-TP correlation [44]. However, the calculated uncertainty was low relative to the standard deviation at each temperature step. This was most likely due to bubble interference with the measurement that is not accounted for in the uncertainty propagation. When measuring non-actinide–bearing salts using x-rays, bubbles cannot be resolved because the salt is mostly transparent to the x-rays. Several lessons were learned from this measurement, mainly involving minimizing gas entrainment within the salt through a combination of proper purification and heat treatment of both the salt and the crucible before the measurement takes place.

2.2 VARIABLE GAP APPARATUS

2.2.1 System Overview and Working Principles

At ORNL, thermal conductivity measurements of molten salts are performed using the variable gap technique developed in 1973 by Cooke [45] and adapted by Gallagher [29, 30]; the system developed by Gallagher is considered herein. The variable gap technique is a steady-state technique involving careful measurement of temperature differences across several different gaps with a fluid specimen with unknown

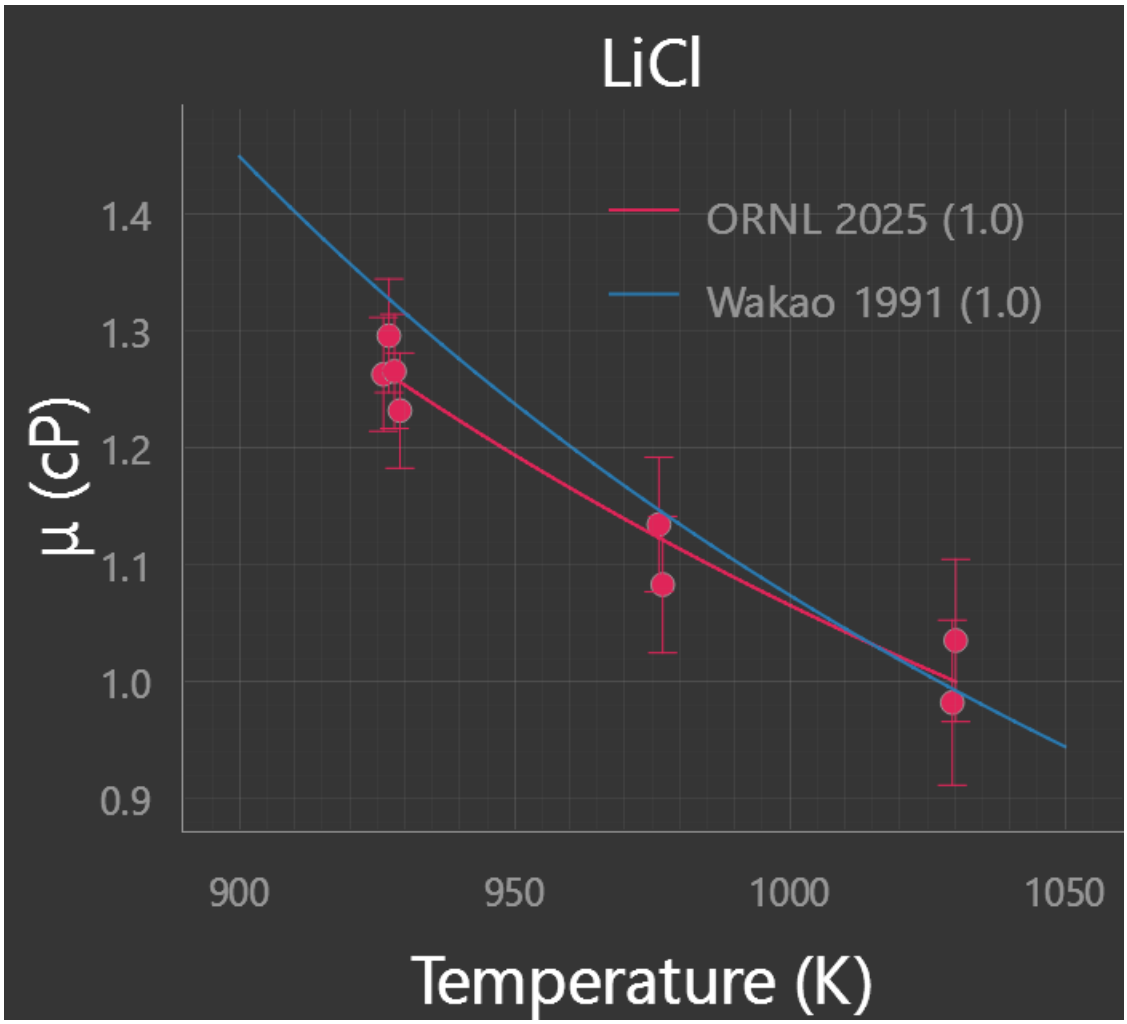

Figure 8. Pure LiCl compared with the MSTDB-TP–recommended correlation in a new stainless steel crucible.

thermal conductivity while driving a known heat flux across. The main advantage of a variable gap apparatus compared with other steady state techniques is that because the length of material being measured can be changed, the ΔT contribution purely by the measured material can be measured. This allows the static components of the system (e.g., steel, thermocouples, insulators) to be effectively ignored when performing the analysis. Using the electrical circuit analog, the system can be described using Figure 9, in which T_{upper} and T_{lower} represent the temperatures, which are measured by the probes located on the upper and the lower ends of the specimen, respectively. Also, $R_{th,upper}$ and $R_{th,lower}$ are the thermal resistances associated with the material between the probes and the specimen, located on the upper and lower ends of the specimen, respectively. These resistances are considered "fixed" because they do not effectively change during the course of the experiment. The specimen itself (salt liquid) has three heat transfer mechanisms; therefore, it should have three resistances in parallel: radiation $R_{th,rad}$, conduction $R_{th,cond}$, and convection $R_{th,conv}$. Careful consideration has been taken to understand each heat transfer mechanism's effect on the experiment.

In standard steady-state thermal conductivity systems, convective cells that form along hot and cold leg channels are major problems because they can be difficult to characterize and can lead to other unnecessary heat losses within the system. However, the decision of a small gap size (<0.3 mm) was to address the issue of convective cells forming within the measurement area. The Rayleigh number (Ra) is a dimensionless number used to describe the effects of buoyancy driven flow:

$$Ra = \frac{g\alpha x^3 C_p \rho^2}{\kappa \eta}. \tag{2}$$

A limit of Ra < 1,708 is based on multiple works [46–48] for negligible convective cell generation. This limit is conservative because, in these works, the heat source is at the bottom, which is more likely to cause buoyancy-driven flow; whereas, in the variable gap experiment it is at the top. Both the gap size and temperature differences are well below the limits considered (1–2 mm and 20°C, respectively). Detailed simulations and explanations are further discussed in Gallagher et al. [29]. With these assumptions, convection can be considered negligible for the experimental conditions that are present.

Solving for the remaining resistances, the total fixed resistances in the system can be defined as

$$R_{fixed} = R_{upper} + R_{lower}, \tag{3}$$

and the total variable resistance in the system is defined as

$$1/R_{var} = 1/R_{cond} + 1/R_{rad}, \tag{4}$$

where the total resistance in the system is

$$R_{tot} = R_{fixed} + R_{var}. \tag{5}$$

Solving and substituting yields

$$R_{tot} = R_{fixed} + \frac{R_{cond} R_{rad}}{R_{cond} + R_{rad}}. \tag{6}$$

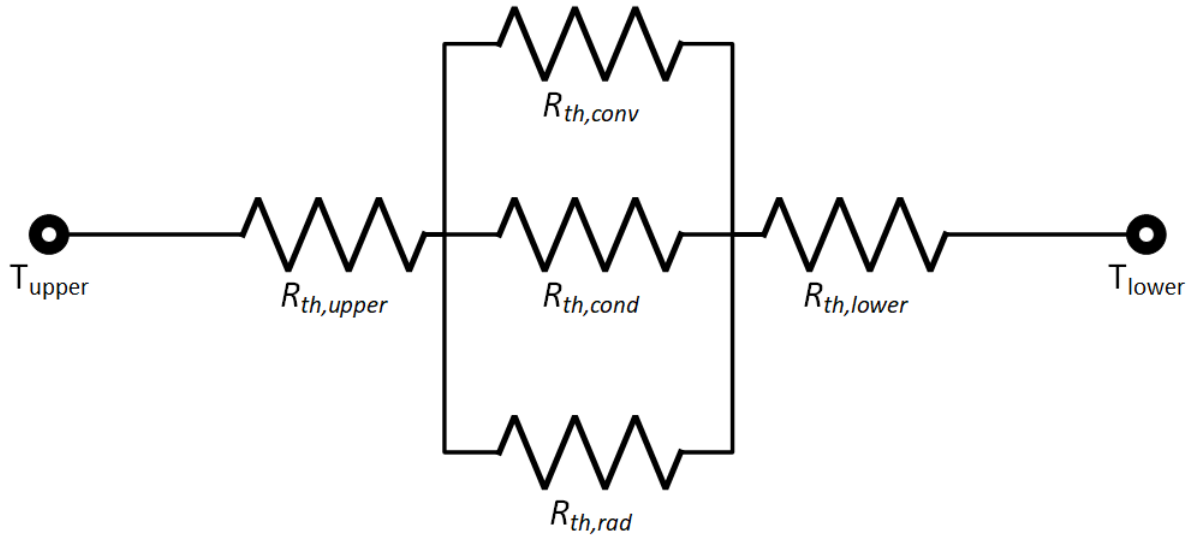

Figure 9. Circuit diagram describing the electrical analog to the thermal resistances associated with the variable gap technique.

The absolute total thermal resistance is defined as

$$R_{tot} = \frac{\Delta T}{Q_{tot}}, \tag{7}$$

where

$$Q_{tot} = Q_{rad} + Q_{cond}, \tag{8}$$

where Q_{rad} is the energy transferred through the sample by radiative heat transfer, and Q_{cond} is the energy transferred by conduction. The conductive resistance can be defined as

$$R_{cond} = \frac{x}{kA}. \tag{9}$$

The radiative resistance depends on the sample being measured. Whereas a transparent medium doesn't directly depend on the sample thickness, the temperature difference between the hot and cold regions will change with specimen temperature. In a salt measurement, the salt is considered optically thin but participating, and the amount absorbed will depend on x. Therefore, we can assume R_{rad} is a function of x in both cases. Taking the derivative with respect to x gives the following:

$$\frac{d}{dx}(R_{tot}) = \frac{R_{rad}^2 R'_{cond} + R_{cond}^2 R'_{rad}}{(R_{cond} + R_{rad})^2}. \tag{10}$$

Substituting in R_{cond},

$$\frac{d}{dx}(R_{tot}) = \frac{\frac{R_{rad}^2}{kA} + \frac{x^2}{k^2A^2}R'_{rad}}{(\frac{x}{kA} + R_{rad})^2}. \tag{11}$$

In a case in which R_{tot} is linear, Eq. (11) must be constant with respect to x. Neglecting x terms,

$$\frac{d}{dx}(R_{tot}) = \frac{1}{kA}. \tag{12}$$

Therefore, by measuring ΔT and Q at different gap sizes and by measuring the slope of the line, if the result is linear, the conductivity of the salt can be determined.

2.2.2 Thermal Conductivity Containment Calibration

The largest challenge faced by this experimental process is the accurate determination of Q across different experimental conditions and salt specimens. The issues arise because heat shunting (i.e., axial and radial heat losses) is especially sensitive to different furnace temperatures, cooling air pressure, fluid measurement, insulation, and main and guard power heating. A parametric study of heat shunting effects on the variable gap apparatus using helium as a standard specimen found that Q_{cond} is a function of $\Delta T_{spec}(x)$ and $T_{furnace}$ and is presented as $Q_{tot}(\Delta T_{spec})$. Experimentally, this means that regardless of the experimental conditions (insulation, furnace temperature, heater power), if two measurements have the same ΔT_{spec} and $T_{furnace}$, then the power available for conduction (Q_{cond}) will be the same.

Therefore, each containment is calibrated extensively using helium to map out the ΔT_{spec} expected for the different salt measurement temperatures. The experimental setup is maintained as constant as possible between measurements (e.g., insulation, thermocouple placement, gap measurement, main and guard power heating); furnace temperature and cooling air pressure are the only two variables changed to achieve different ΔT_{spec}. To solve for Q_{cond}, each measurement needs to be corrected for Q_{rad}, which can be described by the Stefan-Boltzmann law:

$$Q_{rad} = \frac{\sigma(T_1^4 - T_2^4)\varepsilon}{2 - \varepsilon} A \tag{13}$$

where T_1 is the top plate temperature, T_2 is the bottom plate temperature, A is the area of both plates, and ϵ is the emissivity. This equation assumes infinite parallel plates and radial heating uniformity. The emissivity was assumed to be 0.5 because the plates had been reheated, cooled, and exposed to salt several times from the initial polishing.

With a known helium conductivity, Q_{tot} can be measured, and Q_{cond} can be solved for.

Calibration results for a variable gap apparatus constructed in Inconel are shown in Figure 10. To prevent a gap bias, $\Delta T_{spec}(0.15mm)$ and Q_{rad} are taken at a gap of 0.150 mm for both the plotting and solving of Q_{cond}. As seen in Figure 10, Q_{cond} is highly dependent on the furnace temperature. For temperatures 700°C and below, the trend with respect to ΔT_{spec} is more or less linear. The trend at 800°C starts to greatly deviate. This is expected because the T^4 scaling of Q_{rad} has a much greater effect at higher furnace temperatures. Therefore, when choosing Q_{cond} in a salt experiment, both furnace temperature and ΔT_{spec} need to be considered.

2.2.3 Salt Measurement Process

The salt measurement procedure is depicted in Figure 11. After the calibration process, the containment is heated and baked out under vacuum to remove residual oxygen and moisture from all the components. The

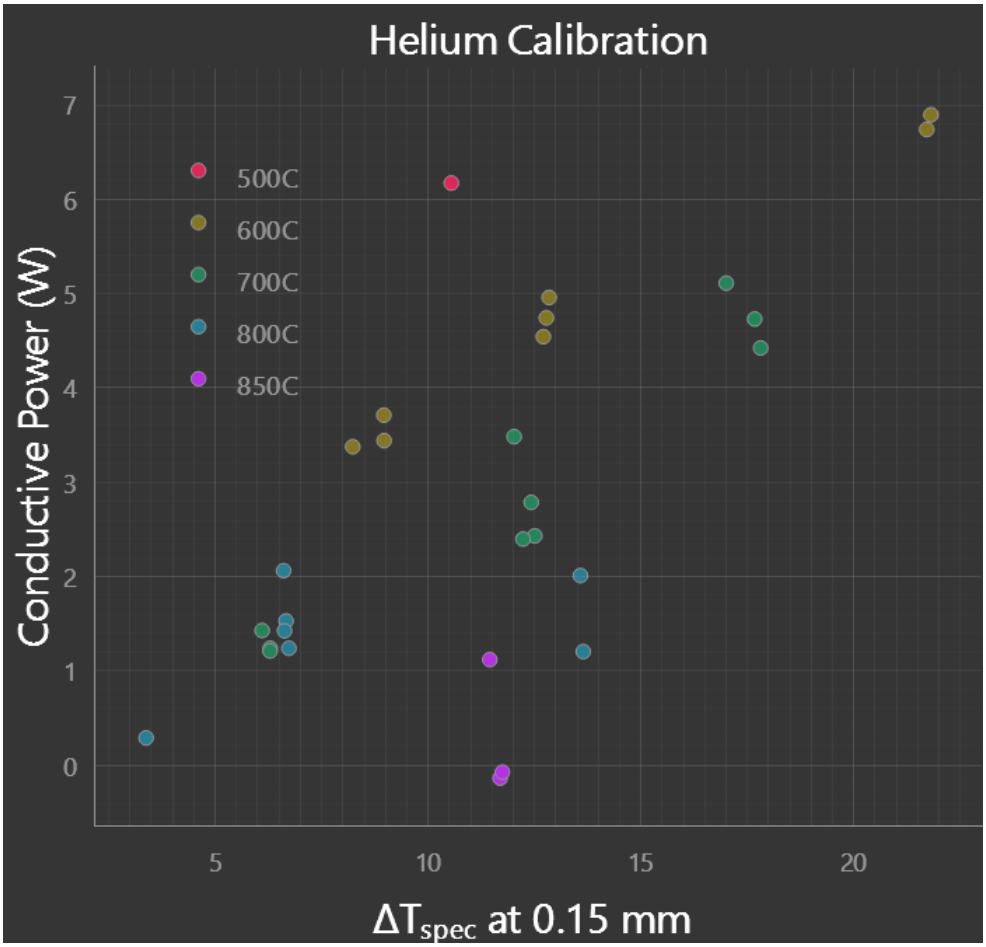

Figure 10. Q_{cond} **across measurement section at a gap size of 0.15 mm for Inconel containment (fluoride containment) as determined through calibration with helium at different furnace temperatures.**

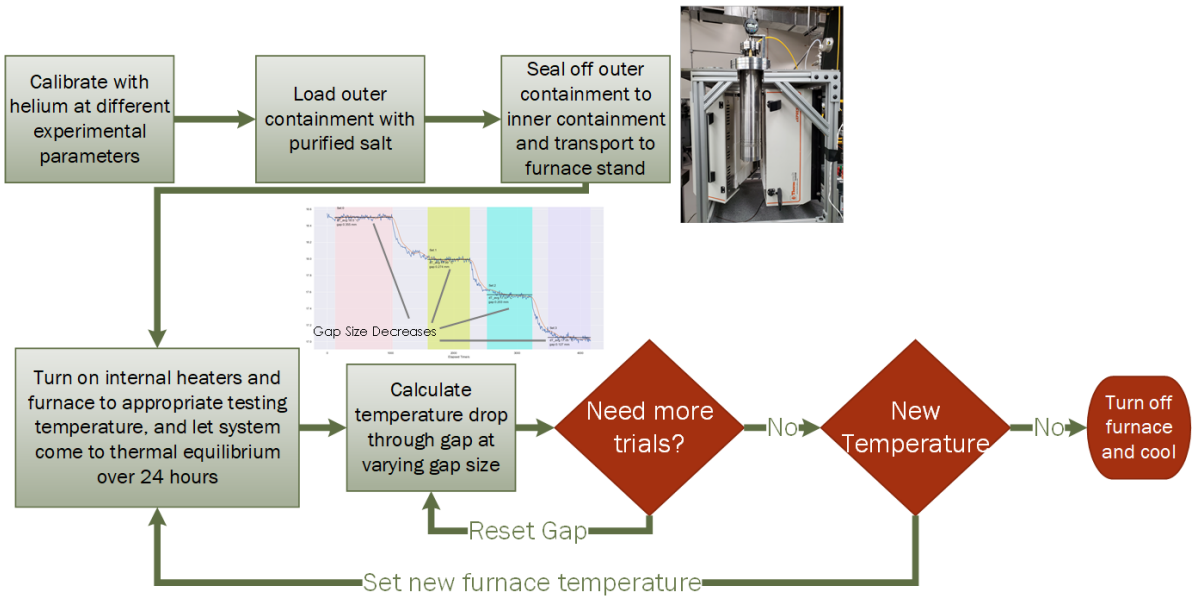

Figure 11. Flowchart for measuring salt in the variable gap apparatus [31].

containment is then transferred into a glove box, where the salt is loaded into the outer containment, and the apparatus is sealed. The apparatus is then placed into the furnace stand, insulated, and brought to measurement temperature with both furnace and internal heaters on. After 24 h of run time, the measurement can then begin: the gap is varied from about 0.350 mm to about 0.100 mm, with time allotted at each gap so the temperature can stabilize and be measured. The gap can be reset to allow for multiple trials. For each new measurement temperature, thermal equilibrium is allowed over a full day. From the measurement data, the temperatures at the top and bottom plates are subtracted to get ΔT_{spec} over time. Gaps can be identified from the flat portions in the data. Using the calibration curve, Q_{cond} can be determined from $T_{furnace}$ and $\Delta T_{spec}(0.150mm)$. Adding Q_{rad} to get Q_{tot}, the resistance can be calculated for each gap. The inverse of the slope of this line is the conductivity.

3. RESULTS

3.1 SAMPLE SYNTHESIS AND CHARACTERIZATION

The NaF-UF_4 (78–22 mol%) and NaF-KF-UF_4 (57-16.04-26.91 mol%) salts were synthesized and purified at Pacific Northwest National Laboratory (PNNL) and Virginia Tech (VT), respectively, via hydrofluorination. Regarding the NaF-UF_4, the compound Na_3UF_7 was crystallized from a 22.2 mol% UF_4 mixture; the starting materials include NaF (Thermo Scientific 99.99%), and UF_4 from PNNL house supplies. The synthesis was carried out in a 9 inch tall nickel sleeve fitted into a Hastelloy-C276 structural containment. The dry salt was heated in the reactor containment, under vacuum at 120°C for 1 h. The temperature was raised to 250°C for another hour under vacuum. Anhydrous HF gas (Synquest Laboratories, Alachua, Fl) was used as a desiccant. Above 250°C, the gas was passed into the dry salt at ≈50 mL/min during programmed heating up to melt. The HF sparger was placed into the melt at 650°C with the HF flow on. Ultra-high-purity Argon (OXARC, Pasco, Wa) was passed through moisture and oxygen traps prior to bubbling it through the same sparger to remove excess HF from the melt. The argon

sparger was removed from the melt and the reactor was cooled to 400°C over a 1 h period. The reactor was then heated to melt and cooled two more times with dried argon sparging.

Regarding the NaF-KF-UF_4 synthesis, salt purification was conducted in purification vessels under a fume hood. The salt purification process was performed using a controlled heating schedule under Ar gas flow, with HF gas introduced during specific stages. The system was ramped at a constant rate of 5 K/min through temperature intervals of RT-393 K, 393-503 K, 503-723 K, and 723-873 K, with hold times of 8, 4, 5, and 12 hours, respectively. HF gas generated from KHF_2, carried by Ar at a flowrate of 100 cc/min, was introduced during the 5-hour hold at 723 K and the subsequent 12-hour hold at 873 K. After the HF source was deactivated, the system remained at 873 K for an additional 12 hours under Ar flow only. The process concluded with a cooldown to room temperature at a flowrate of 200 cc/min.

The NaF-UF_4 was analyzed via XRD prior to shipment to ORNL for thermal property measurements. An XRD sample of the salt was prepared in (Bruker Airtight specimen holder A100B33) a inert glove box. The diffractometer used was a Rigaku Smart Lab powder X-ray diffractometer equipped with a Cu anode X-ray source and a 2D-detector. Phase ID was executed using the Bruker EVA version 6 search match software that interfaces with the International Center for Diffraction Data, Powder Data File 5 database (commonly referred to as ICDD PDF-5). A single phase identified as β-Na_3UF_7 is indicated by the fit to the powder pattern. The presence of free NaF, UF_4, UO_2 , U_3O_8 or UO_2F_2 were not observed.

The NaF-KF-UF_4 was analyzed via inert gas fusion and ICP-MS prior to shipment to ORNL. Inert gas fusion analysis was performed using a Bruker G6 Leonardo to measure oxygen and hydrogen concentrations in salt samples. At least five independent samples were packed in tin capsules within the glovebox and analyzed separately for oxygen and hydrogen. Calibration was carried out using titanium reference pins from Alpha Resources, producing a calibration curve with an R^2 value greater than 0.995. Elemental analysis was conducted using an Agilent 7800 ICP-MS operating in helium collision mode. Three independent salt samples were digested in 1 M nitric acid using polypropylene centrifuge tubes. Calibration was performed with a multi-element standard solution (71A) from Inorganic Ventures, yielding an R^2 value greater than 0.9995. The ICP-MS results revealed that the sample was 99.95 % pure (trace metal masis), while the inert gas fusion results revealed the sample contained 817 ±167 ppm oxygen, and 19 ±7 ppm hydrogen.

3.2 NAF-UF_4 AND NAF-KF-UF_4 VISCOSITY

NaF-UF_4 (78–22 mol%) and NaF-KF-UF_4 (57–16.04–26.91 mol%) salts were measured using SS-316 crucibles. These crucibles were predried at 300°C at vacuum for a minimum of 3 h, sealed and transported into the glove box, where each salt was loaded into the crucible. Calculations were performed to load the appropriate amount of salt to ensure filling of the entire test section and 1–2 in. of the loading section with liquid salt for two purposes: (1) to prevent gas entrainment of the ball into the measurement section salt as the ball falls into the salt and (2) to allow the ball to come to equilibrium temperature with the salt before it enters the measurement section. Next, 44 g of NaF-UF_4 and 39 g of NaF-KF-UF_4 were loaded into their respective crucibles. The salts were then heated in the furnace for a minimum of 24 h before testing to ensure salt thermal equilibrium and to allow entrained gas to escape. Simply heating the salt was found to be insufficient for removing an appropriate amount of suspended bubbles throughout the salt, and gas entrapment and the formation of bubbles initially posed the major roadblock to performing these measurements. Through a combination of physical perturbations (e.g., vibrations, ball travel, pressure modulations) and cooling and reheating the salt, smaller unresolved suspended bubbles combined into

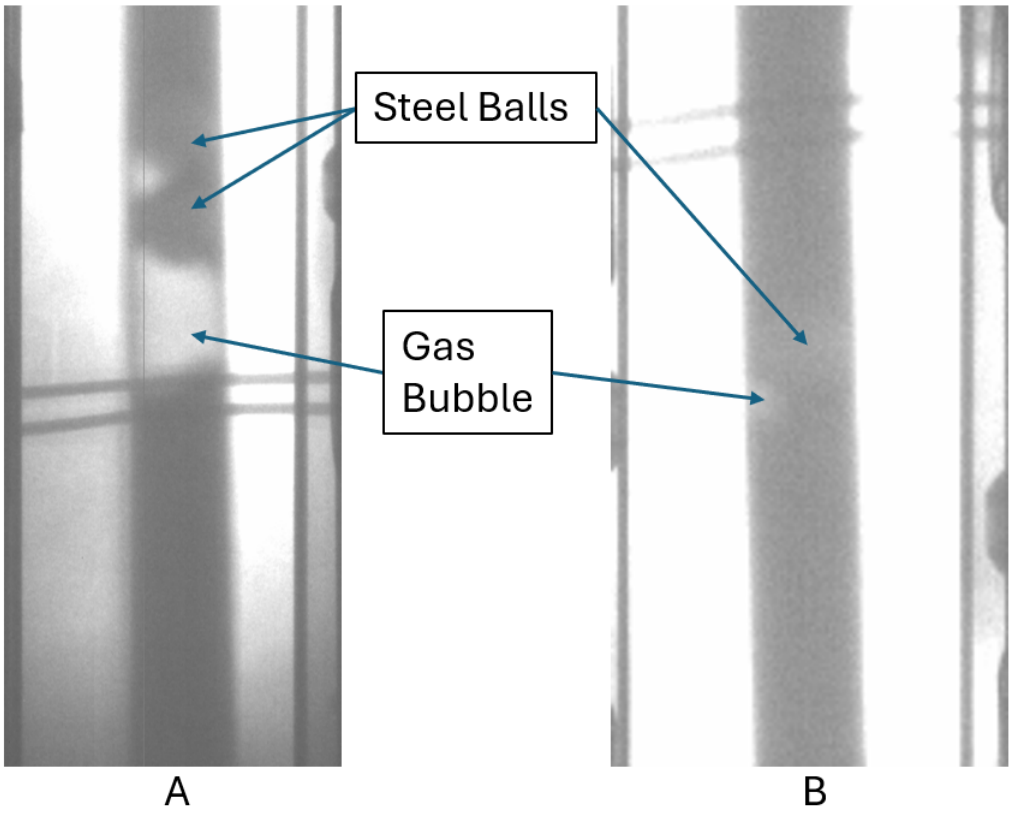

Figure 12. A: Steel balls stuck on a large gas bubble. B: A ball slowed down by a small bubble during a trial.

larger voids and could be removed from the system (Figure 12A). Owing to the relatively high expected viscosity of these salts, high measurement angles were used (>26°) to prevent effects of dynamic versus static friction. The system needed to be vibrated to overcome static friction and to get the ball rolling to terminal velocity. A measurement was considered successful if a ball did not come to a stop within the measurement section, could roll past the x-ray window unassisted, and was not inhibited by bubbles (Figure 12B).

The viscosities of NaF-UF_4 and NaF-KF-UF_4 are shown in Figures 13 and 14, respectively. Densities used in the calculation of viscosity were derived from either experimental data if the exact composition was available or RK estimation methods extrapolated from existing data for the given salt. Each salt is compared with relevant MSTDB-TP reference correlations [37, 49]. The binary salt shows good agreement to Blanke computational trend [37]. The ternary salt is a bit more difficult because the effects of composition differences among three different salts are difficult to predict. The trends show that the measured salt has a higher melting point than that described in Cohen [49], which is to be expected owing to the much lower KF composition. Calculating the melting point using thermochimica and MSTDB-TC, the melting point for the measured mixture is 851 K, compared with the experimentally measured Cohen's mixture of 803 K [34], which fits the hypothesis. Both salts show clear Arrhenius fits to temperatures. Tabulated results and fit parameters are shown for both salts in Tables 1 and 2.

Table 1. NaF-UF_4 (78–22 mol%) viscosity measurements. Densities are calculated using RK extrapolation based on Cohen's measurements [34]

Temperature (K)	Density (g/cm^3)	Viscosity (cP)	Error ± (cP)
1,046.15	3.75323	8.04089	0.266907
1,045.15	3.75427	8.20072	0.402868
1,041.28	3.75829	8.70125	0.322724
1,040.63	3.75897	8.94579	0.310777
986.66	3.8151	10.7292	0.349698
995.06	3.80636	11.8118	0.383246
987.96	3.81375	11.0395	0.357709
935.15	3.86867	13.9636	0.46574
936.47	3.8673	13.2131	0.435501
939.16	3.8645	13.4703	0.442081
940.93	3.86266	14.5347	0.4773
Arrhenius Fit ($Ae^{B/T}$):	A = 0.132	B = 4,366.58	

Table 2. NaF-KF-UF_4 (57–16.04–26.91 mol%) viscosity measurements. Experimental density values of this exact composition were used [50]

Temperature (K)	Density (g/cm3)	Viscosity (cP)	Error ± (cP)
1,025.04	4.18509	8.77235	0.563202
1,024.19	4.18591	8.39294	0.32388
1,023.42	4.18666	8.5372	0.33949
1,024.49	4.18562	8.47664	0.331153
948.97	4.25887	13.5923	0.547278
948.81	4.25903	12.4797	0.5008
950.49	4.2574	13.1376	0.521693
952.28	4.25566	13.8158	0.562041
878.02	4.3277	24.5822	1.01272
880.17	4.32561	23.9629	0.985421
884.52	4.32139	23.7837	0.975715
882.9	4.32296	22.8527	0.932504
Arrhenius Fit ($Ae^{B/T}$):	A = 0.0119	B = 6,696.33	

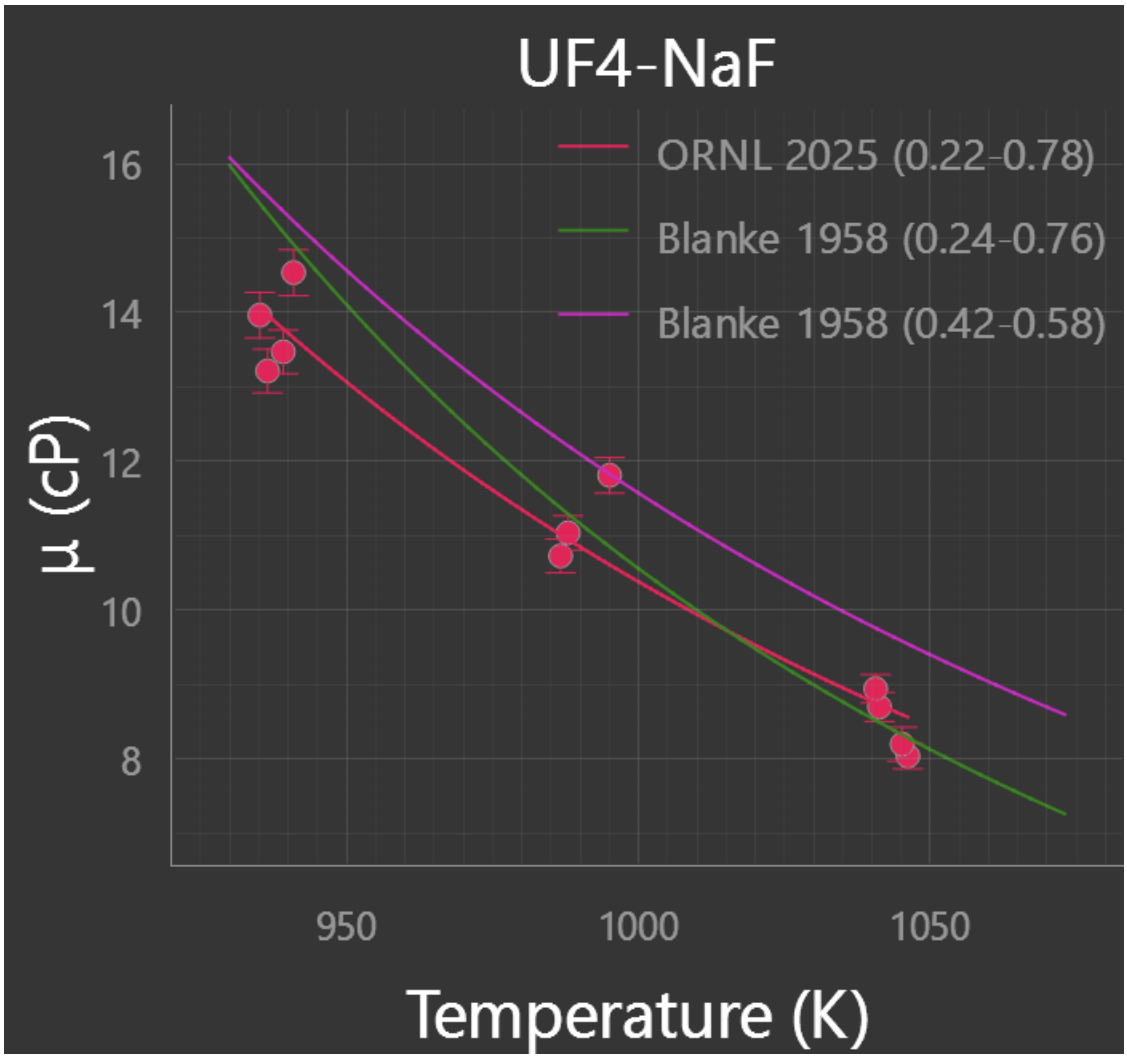

Figure 13. NaF-UF_4 (78–22 mol%) viscosity measured using rolling ball apparatus compared with MSTDB-TP relevant correlations [37].

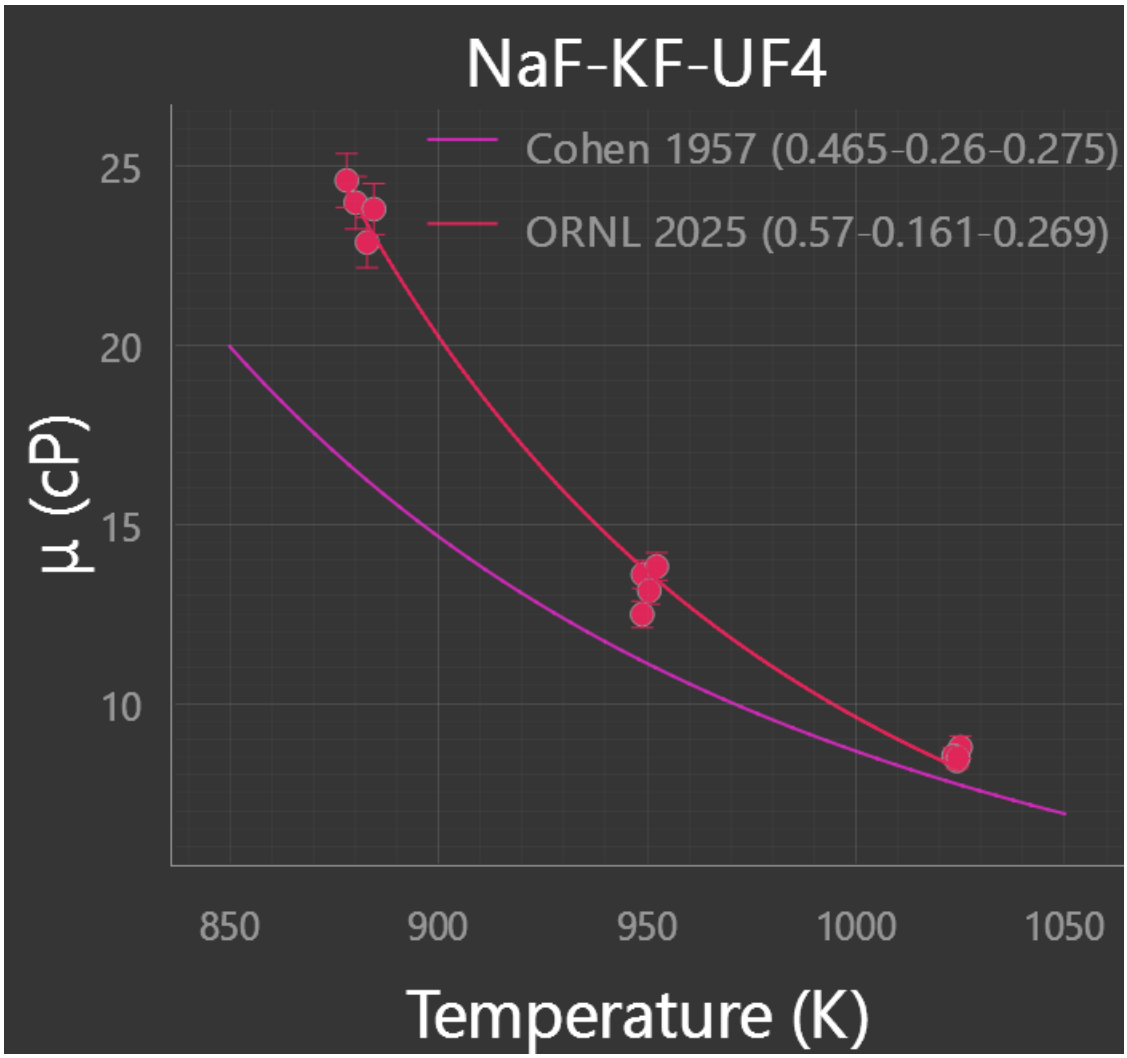

Figure 14. NaF-KF-UF_4 (57-16.0-26.9 mol%) viscosity measured using rolling ball apparatus compared with an MSTDB-TP relevant correlation [49].

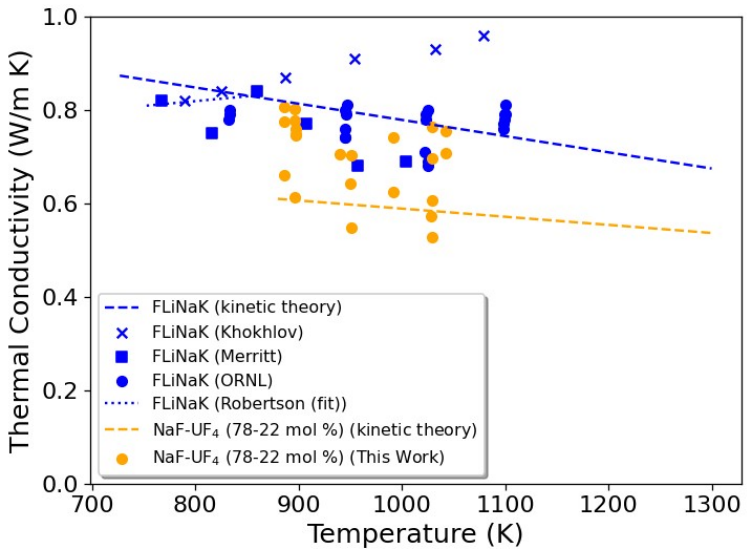

Figure 15. NaF-UF_4 (78–22 mol%) thermal conductivity measured using a variable gap apparatus. The data is compared with a kinetic theory model [20] and with literature data on FLiNaK [30, 41, 51, 52].

3.3 NAF-UF_4 THERMAL CONDUCTIVITY

NaF-UF_4 (78–22 mol%) salt was measured in the Inconel variable gap apparatus. The containment was predried under vacuum at 300°C for 4 h before being transferred to a glove box, where salt was loaded into the containment. The containment was then set up in the furnace, and the salt was heated to measurement temperature for a minimum of 24 h. Measurements were taken at six furnace setpoints: 625, 650, 675, 700, 725, and 775. The measurement took place over 2 weeks, where the system was cooled over the weekend and reheated the next week for safety concerns. Each furnace set point was given an entire night to come to thermal equilibrium before new measurements were made.

The results of the NaF-UF_4 (78–22 mol%) measurement compared with other FliNaK salt thermal conductivity data in the literature [30, 41, 51, 52] and with the predicted kinetic theory [20] model are shown in Figure 15. Compared with the kinetic theory model, the measurements are overpredicting. The data spread is predicted because of instabilities in thermal equilibrium or bubble formation within the salt.

4. IMPROVEMENTS

Several improvements were made to the experimental process for both measurement systems to address increased precision and increased efficiency from start to final measurement. Updates to the viscosity system include a crucible redesign discussed early in this report, an automated glass crucible calibration device, creation of a x-ray image processing GUI, and creation of an analysis code GUI. The variable gap apparatus was slightly redesigned to address redundant features and flanges that caused leaks from the external to internal containment and needlessly complicated the manufacturing process. All the analysis codes for this system were combined, and implemented into a GUI with better visualization features to streamline the large amount of data to process.

4.1 AUTOMATED GLASS CALIBRATION DEVICE

The calibration of glass crucibles requires a significant number of measurements to properly account for the effects of both the diameter mismatch between the ball and the crucible and the effects of Reynolds number on the calibration factor K. This entails the measurement of terminal velocity of four different ball sizes at several different angles in up to four oils, depending on the salts expected to be measured. Each crucible needs to be individually calibrated because of large manufacturing tolerances on the inner diameter of glass tubes and inconsistencies along the length of that inner diameter. Previously, each measurement of dropping balls (consisting of one angle and oil combination) would be videotaped, and the video frames at which each ball crossed set markings at a known length would be found manually. A calibration would typically take multiple days for both measurement and data analysis. Therefore, an automated glass calibration device, shown in Figure 16, was designed and built as part of a student project. This device consists of multiple photointerrupters set up in series along the test section of the crucible that trigger when the ball passes them. These sensors are connected to a Raspberry Pi 4 model B, which records the time at which it receives a signal from a photointerrupter when a ball passes through. Through a GUI programmed on the Raspberry Pi, experimental parameters can be input for each oil/angle combination; once the test is finished, the Raspberry Pi automatically calculates, formats, and outputs the results to a comma-separated value (CSV) file that can be used later for a salt experiment with the calibrated crucible. The amount of time to calibrate one crucible to salt experiment standards using this device is around 3 h, whereas the previous method required several days. These calibrations yield higher quality data because more points along the crucible are measured, giving a better understanding of the inner diameter inconsistencies along the length of the test section.

4.2 VISCOSITY AND THERMAL CONDUCTIVITY ANALYSIS CODE GUIS

Both property measurements require code bases to process the experimental data, apply systematic uncertainty, and output property measurements. Previous approaches to processing data were Python scripts that required significant tinkering to both the experimental records (CSV, Excel documents) and the Python script itself to set experimental parameters correctly, properly fit the data to various expressions via least squares, and compare the data with relevant literature. For a large number of trials, this process takes time and is prone to user error. Therefore, separate comprehensive GUIs were developed for both measurements

The main improvements to thermal conductivity data analysis are the addition of bulk measurement and active visualization of processed data. Previously, each trial being measured required an individual run of the code to produce ΔT vs. time and resistance vs. gap plots, which could be used to identify the thermal conductivity. Within each trial, the gap identification parameters may need to be tuned to properly identify when the gap is changed, requiring repeat runs of the code. The conductivity needs to be manually recorded with other pertinent experimental parameters for both calibration and salt measurement. A proper calibration with multiple furnace temperatures, multiple trials per temperature, and different cooling powers will require hundreds of individual runs of this code. Figure 17 shows several of the features of the GUI. Trials can be added by the folder or individually, treating each trial as an entry to be processed. Each trial's run can be altered to adjust the gap-fitting parameters for different thermal conditions and for gaps to be dropped if outliers occur. When a trial is run, each ΔT vs. time curve and resistance plot along with its associated calculated conductivity can be viewed to ensure the code runs properly. If the code can't fit properly, the trial shows red; it can then be adjusted and run again individually. The final data are shown in a table that can be copied or exported to a CSV file with all the relevant plots of each trial.

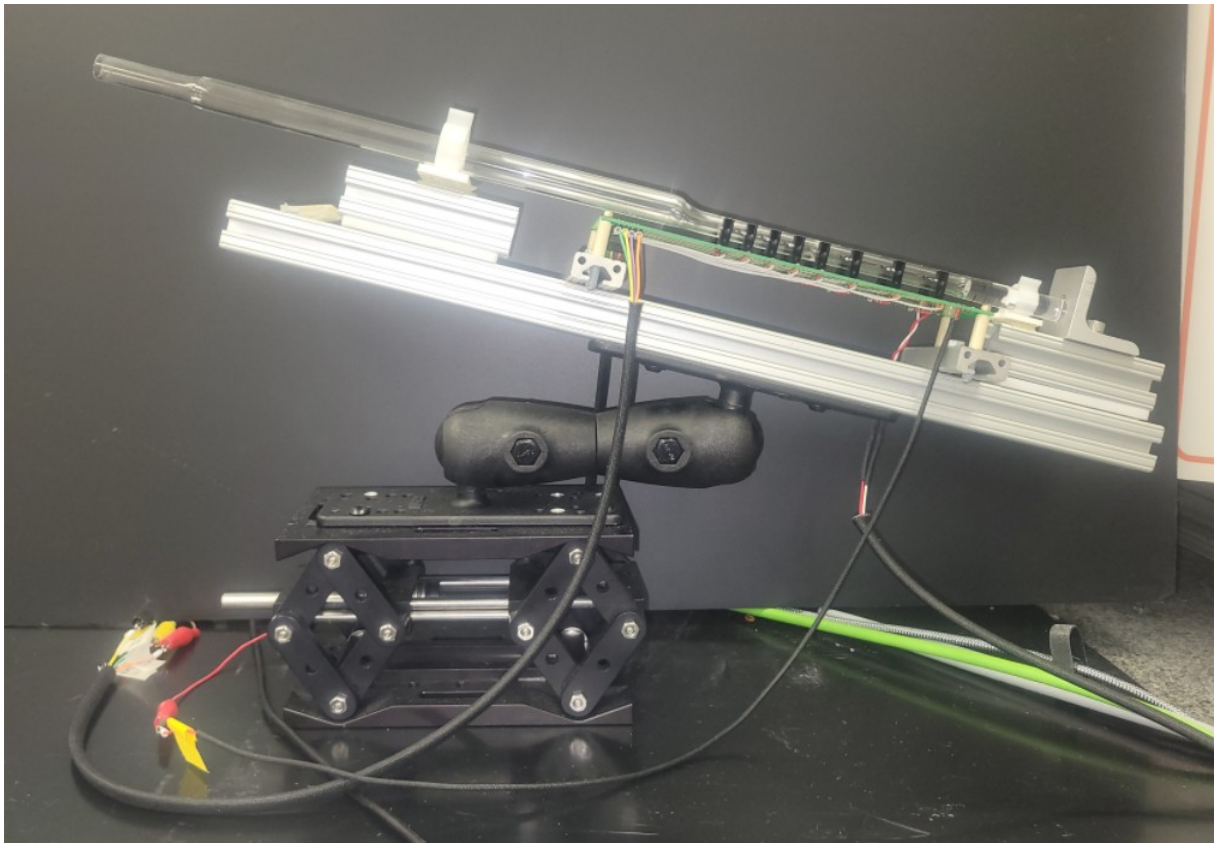

Figure 16. Automatic glass calibration device.

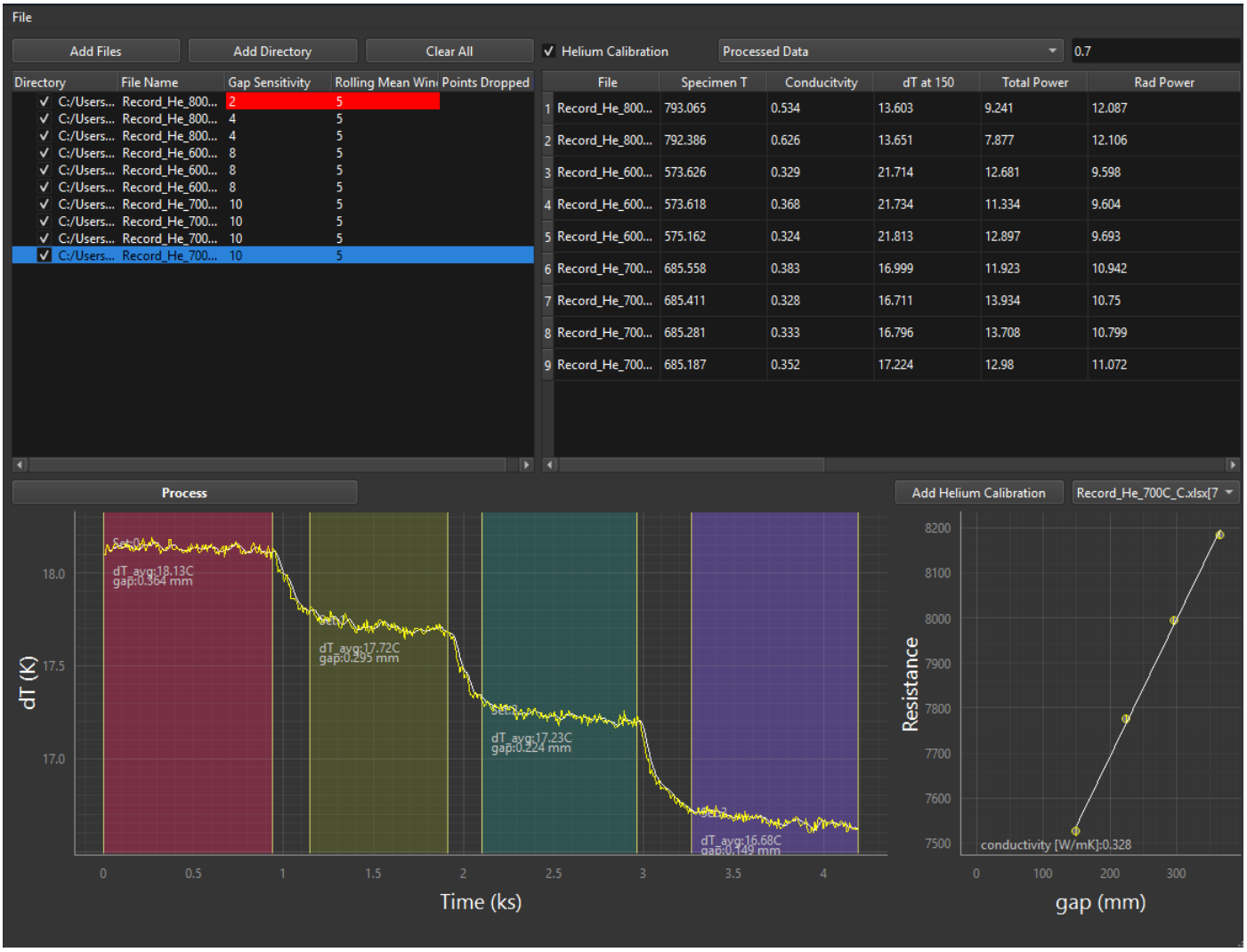

Figure 17. Screenshot of thermal conductivity GUI processing multiple helium calibration trials.

The viscosity GUI incorporates a line of thought similar to that of the thermal conductivity GUI in that it streamlines data analysis and visualization (Figure 18). Instead of two codebases, the viscosity GUI allows the selection of processing a glass or steel crucible. It automatically imports calibration data from the appropriate files (for either a glass or steel crucible), and it tabulates and plots the data for consistency. Because these viscosity measurements need density for calculation, MSTDB-TP is incorporated into this GUI through Saline, and experimental density parameters can be automatically imported into the calculation for the desired composition and salt. If the desired composition is not present in MSTDB-TP, it can be approximated using Saline's RK estimation capabilities or can be input manually. Viscosity data present in MSTDB-TP can be imported and plotted against calculated experimental data. All tabulated or plotted data can be copied or exported into appropriate formats.

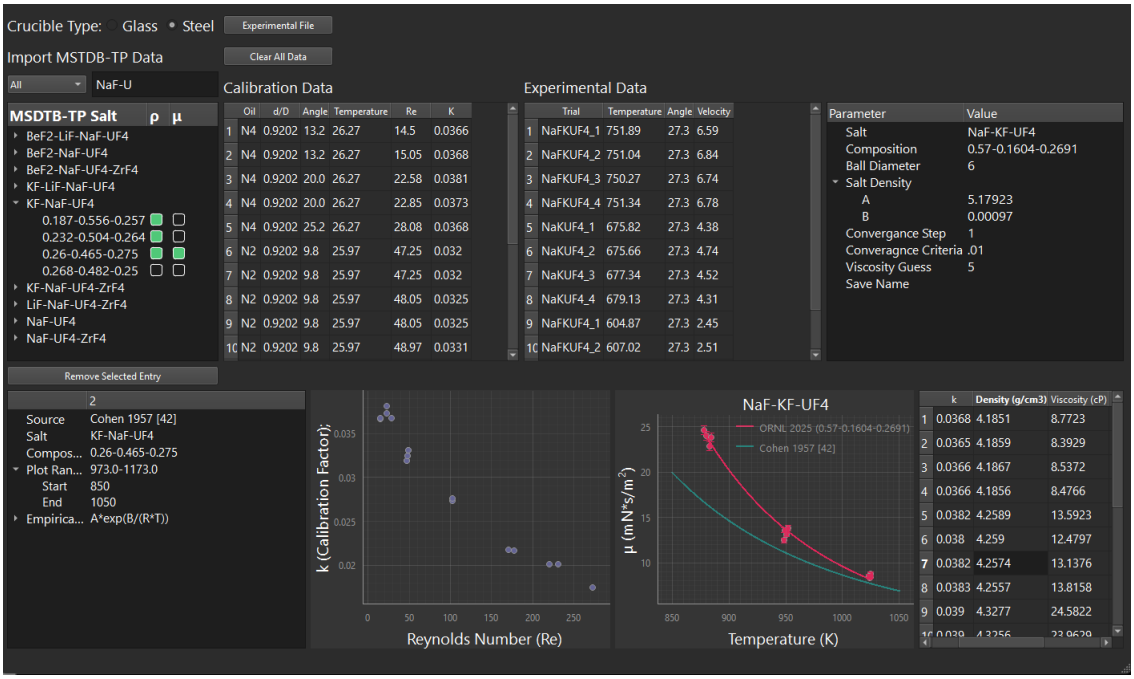

Figure 18. Screenshot of viscosity GUI processing NaF-KF-UF_4 (0.57–0.160–0.269 mol%) salt data.

4.3 VISCOSITY IMAGE PROCESSING GUI

As part of a student project, the processing of x-ray images was updated with the creation of a GUI. Previously, each frame of the x-ray image file acquired from the detector plate was copied into an image stack and processed in ImageJ. The image was thresholded against the ball, which was tracked in each frame. The pixel distances were extracted, and distances could be calculated from a known reference distance in the image. These distances were then copied into another document to be processed.

The GUI combines all of the previous steps into one program, shown in Figure 19. The HIS file is directly chosen, and all the relevant experimental parameters (either calibration or experiment) are auto-extracted from the file name. A scale can be drawn on the image from the reference points in the experiment. The program will try to find the ball automatically based on the diameter given in the program (green circle in the figure). If the program is unsuccessful, users can manually chose the ball's position using a template based on the size of the ball (red circle in the figure). All points recorded are shown in a table on the GUI, with the running average velocity displayed. When the process is finished, the data are auto-formatted for an oil calibration and can either be exported to a CSV file or copied into another document.

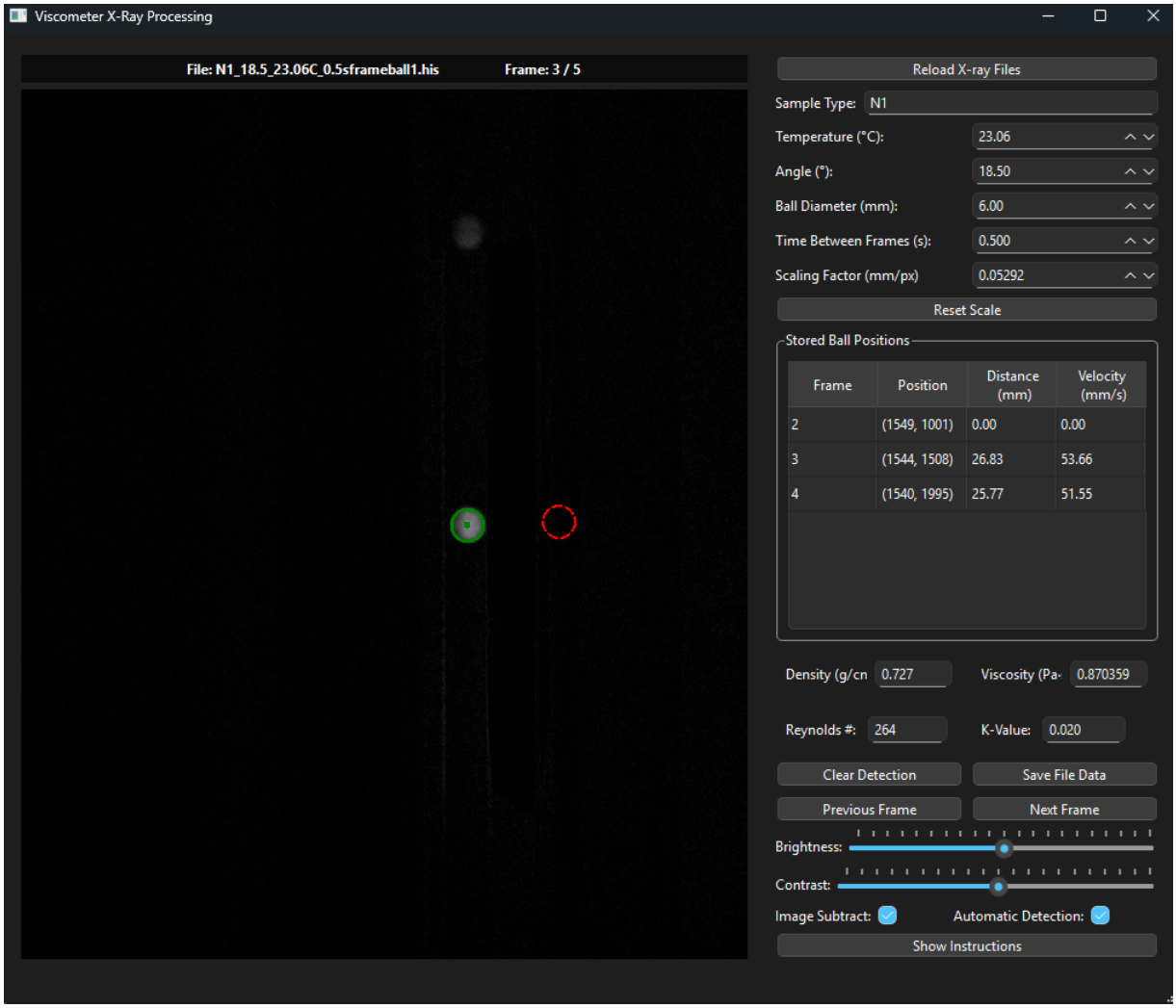

Figure 19. Screenshot of x-ray image processing GUI identifying a ball traveling through an SS-316 crucible in N1 oil.

5. CONCLUSION

The experimental viscosity and thermal conductivity data collected in this study—for NaF-UF_4 (78–22 mol%) and NaF-KF-UF_4 (57–16.04–26.91 mol%)—serve to fill key gaps for transport properties of actinide fluorides in MSTDB-TP. The thermal conductivity data collected for NaF-UF_4 (78–22 mol%) provide quantitative evidence of a tendency for actinide-bearing fluorides, relative to their carrier salts or typical fluoride coolant salts, to have lower thermal conductivity values as a result of the addition of actinides into the melt. Comparison with kinetic theory models shows general quantitative consistency in the difference between the thermal conductivities in NaF-UF_4 (78–22 mol%) and FLiNaK. Viscosity data collected for both NaF-UF_4 (78–22 mol%) and NaF-KF-UF_4 (57–16.04–26.91 mol%) show expected Arrhenius relationships as a function of temperature, indicating Newtonian fluid behavior in the temperature regimes studied. Despite compositional differences, the data collected herein show reasonable agreement with legacy viscosity data for both salt systems. In general, the actinide-bearing fluoride mixtures studied herein have relatively low thermal conductivities and relatively high viscosities compared with the same properties of typical coolant fluoride salts at these temperatures (e.g., FLiNaK, FLiBe). These quantitative differences should be factored into design considerations for developing MSRs, which will use high-fissile loading in their fuel salts. Note that significant efforts were also reported here on the advancement of data processing techniques, implementation of GUIs, automation of calibration procedures, and simplification of crucible manufacturing. These efforts will result in higher throughput capabilities so that actinide-bearing salts can be more rapidly assessed in future studies, with improved characterization of uncertainty margins.

6. REFERENCES

[1] Anthony Birri, Nick Termini, Kevin Garland, Shay Chapel, Hunter Andrews, Paul Rose Jr., and N. Dianne Bull Ezell. FY23 Progress Report on Viscosity and Thermal Conductivity Measurements of Molten Salts. Technical report, Oak Ridge National Lab.(ORNL), Oak Ridge, TN (United States), 2023. ORNL/TM-2023/3048.

[2] Toni Y Karlsson, Scott C Middlemas, Manh-Thuong Nguyen, Michael E Woods, Kevin R Tolman, Vassiliki-Alexandra Glezakou, Steven D Herrmann, Juliano Schorne-Pinto, Ryan D Johnson, Shawn E Reddish, et al. Synthesis and Thermophysical Property Determination of NaCl-PuCl3 Salts. *Journal of Molecular Liquids*, page 122636, 2023.

[3] MA Rose, LD Gardner, TT Lichtenstein, SA Thomas, and E Wu. Property Measurements of NaCl-UCl3 and NaCl-KCl-UCl3 Molten Salts. Technical report, Argonne National Laboratory (ANL), Argonne, IL (United States), 2023. ANL/CFCT-22/45 Rev. 1.

[4] Stephen Scott Parker, A Long, C Lhermitte, S Vogel, M Monreal, and JM Jackson. Thermophysical properties of liquid chlorides from 600 to 1600 K: Melt point, enthalpy of fusion, and volumetric expansion. *Journal of Molecular Liquids*, 346:118147, 2022.

[5] Jason Lonergan, Vitaliy Goncharov, Michaella Swinhart, Kyle Makovsky, Mark Rollog, Bruce McNamara, Richard Clark, Derek Cutforth, Christopher Armstrong, Xiaofeng Guo, et al. Thermodynamic investigation of the NaCl-KCl salt system from 25 to 950ř C. *Journal of Molecular Liquids*, 391:122591, 2023.

[6] Kyle Makovsky, Michaella Harris, Ji-Hye Seo, Kent Detrick, Jose Marcial, Dallin Barton, and Jacqueline Roye. Experimental Investigation into Select Thermophysical Properties of the Potassium-Magnesium Chloride Salt System for Molten Salt Reactors. Technical report, Pacific Northwest National Laboratory, 2024. PNNL-37190.

[7] LD Gardner, KA Chamberlain, and MA Rose. Property measurements of lif-naf-kf molten salts doped with surrogate fission products. Technical report, Argonne National Laboratory (ANL), Argonne, IL (United States), 2024.

[8] Manh-Thuong Nguyen, Michael E Woods, Juliano Schorne-Pinto, Nick H Erfurth, Scott C Middlemas, and Toni Karlsson. Thermophysical properties of nacl–ucl3–pucl3 molten salts: A combined computational and experimental study. *ACS Applied Energy Materials*, 8(10):6482–6491, 2025.

[9] Andrew C Strzelecki, S Scott Parker, Shane C Mann, David C Arellano, Sarah M Hickam, S Douglas Ware, Nathan A Conroy, Hakim Boukhalfa, Titus YP De Jong, David A Andersson, et al. Determination of thermochemical properties of the molten pucl3-nacl eutectic mixture by high-temperature drop calorimetry. *Journal of Molecular Liquids*, 424:127073, 2025.

[10] Jiri Krepel and Kevin J Kramer. TerraPower fast chloride reactor. In *Molten Salt Reactors and Thorium Energy*, pages 953–972. Elsevier, 2024.

[11] Andrei Rykhlevskii. Kairos power pebble bed reactor. In *Molten Salt Reactors and Thorium Energy*, pages 945–952. Elsevier, 2024.

[12] Sarah Elizabeth Creasman, Visura Pathirana, and Ondrej Chvala. Sensitivity study of parameters

important to Molten Salt Reactor Safety. *Nuclear Engineering and Technology*, 55(5):1687–1707, 2023.

[13] Edward Blandford, Kyle Brumback, Lambert Fick, Craig Gerardi, Brandon Haugh, Elizabeth Hillstrom, Kevin Johnson, Per F. Peterson, Floren Rubio, Fatih S. Sarikurt, Sonat Sen, Haihua Zhao, and Nicolas Zweibaum. Kairos Power thermal hydraulics research and development. *Nuclear Engineering and Design*, 364:110636, 2020. ISSN 0029-5493. doi: https://doi.org/10.1016/j.nucengdes.2020.110636. URL https://www.sciencedirect.com/science/article/pii/S0029549320301308.

[14] Lars Jorgensen. 19 - ThorCon reactor. In Thomas J. Dolan, editor, *Molten Salt Reactors and Thorium Energy*, pages 557–564. Woodhead Publishing, 2017. ISBN 978-0-08-101126-3. doi: https://doi.org/10.1016/B978-0-08-101126-3.00019-1. URL https://www.sciencedirect.com/science/article/pii/B9780081011263000191.

[15] Kirk Sorensen. Liquid-Fluoride Thorium Reactor Development Strategy. In Jean-Pierre Revol, Maurice Bourquin, Yacine Kadi, Egil Lillestol, Jean-Christophe de Mestral, and Karel Samec, editors, *Thorium Energy for the World*, pages 117–121, Cham, 2016. Springer International Publishing.

[16] K.A. Triplett, S.M. Ghiaasiaan, S.I. Abdel-Khalik, A. LeMouel, and B.N. McCord. Gasliquid two-phase flow in microchannels: Part ii: void fraction and pressure drop. *International Journal of Multiphase Flow*, 25(3):395–410, 1999. ISSN 0301-9322. doi: https://doi.org/10.1016/S0301-9322(98)00055-X. URL https://www.sciencedirect.com/science/article/pii/S030193229800055X.

[17] Zhiya Qiao, Lijun Yan, Zhanmin Cao, and Yunan Xie. Surface tension prediction of high-temperature melts. *Journal of Alloys and Compounds*, 325(1):180–189, 2001. ISSN 0925-8388. doi: https://doi.org/10.1016/S0925-8388(01)01362-7. URL https://www.sciencedirect.com/science/article/pii/S0925838801013627.

[18] Nick Termini, Anthony Birri, Shane Henderson, and N. Dianne Bull Ezell. An Overview of the Molten Salt Thermal Properties Database–Thermophysical, Version 2.1.1 (MSTDB-TP v.2.1.1). Technical report, Oak Ridge National Lab.(ORNL), Oak Ridge, TN (United States), 2023.

[19] AE Gheribi, D Corradini, L Dewan, P Chartrand, C Simon, Paul A Madden, and M Salanne. Prediction of the thermophysical properties of molten salt fast reactor fuel from first-principles. *Molecular Physics*, 112(9-10):1305–1312, 2014.

[20] A Birri, R Chesser, N Termini, JC Numbers, Kevin Garland, and MA Rose. Reference correlations for the density and viscosity of molten alkali and alkaline earth fluoride salts. *Journal of Physical and Chemical Reference Data*, 54(2), 2025.

[21] Juliano Schorne-Pinto, Mina Aziziha, Hunter B Tisdale, Amir M Mofrad, Anthony Birri, Matthew S Christian, Johnathon C Ard, Ronald E Booth, Jacob A Yingling, Jorge Paz Soldan Palma, et al. Thermal Property Modeling and Assessment of the Physical Properties of FLiNaK. *ACS Applied Energy Materials*, 7(9):4016–4029, 2024.

[22] Xue-Hui An, Jin-Hui Cheng, Hui-Qin Yin, Lei-Dong Xie, and Peng Zhang. Thermal conductivity of high temperature fluoride molten salt determined by laser flash technique. *International Journal of Heat and Mass Transfer*, 90:872–877, 2015.

[23] D Tolbaru, Rodica Borcan, and Stefania Zuca. Viscosity measurements on molten salts with an oscillating cup viscometer: viscosity of molten KNO3 and NaCl. *Berichte der Bunsengesellschaft für physikalische Chemie*, 102(10):1387–1392, 1998.

[24] MA Rose, E Wu, and MA Williamson. Thermophysical Property Measurements: Improved Density, Viscosity and Thermal Diffusivity Methods. Technical report, Argonne National Lab.(ANL), Argonne, IL (United States), 2020.

[25] Anthony Birri, Nicholas Termini, Paul Rose, Shay Chapel, Hunter Andrews, and N. Dianne Bull Ezell. Development and demonstration of a rolling ball viscometer for molten salts with near-minimum liquidus NaClKCl. *Thermal Science and Engineering Progress*, 44:102029, 2023. ISSN 2451-9049. doi: https://doi.org/10.1016/j.tsep.2023.102029. URL https://www.sciencedirect.com/science/article/pii/S2451904923003827.

[26] N Ezell, Ryan C Gallagher, Nicholas Russell, Alex Martin, Jake W Mcmurray, and Abbey McAlister. Thermophysical Property Measurements on Salt Mixture. Technical report, Oak Ridge National Laboratory (ORNL), Oak Ridge, TN (United States), 2020.

[27] N Ezell, Ryan C Gallagher, Can Agca, and Jake McMurray. Thermal Property Characterization of Molten Salt Reactor–Relevant Salts. Technical report, Oak Ridge National Lab.(ORNL), Oak Ridge, TN (United States), 2021.

[28] Tony Birri, Ryan C Gallagher, Nick Russell, Nick Termini, Paul Rose Jr, and N Dianne Ezell. FY22 Progress Report on Viscosity and Thermal Conductivity Measurements of Molten Salts. Technical report, Oak Ridge National Lab.(ORNL), Oak Ridge, TN (United States), 2022.

[29] Ryan C Gallagher, Anthony Birri, Nick Russell, and N Dianne B Ezell. Design and performance of a variable gap system for thermal conductivity measurements of high temperature, corrosive, and reactive fluids. *International Journal of Heat and Mass Transfer*, 192:122763, 2022.

[30] Ryan C Gallagher, Anthony Birri, Nick G Russell, Anh-Thu Phan, and Aïmen E Gheribi. Investigation of the thermal conductivity of molten LiF-NaF-KF with experiments, theory, and equilibrium molecular dynamics. *Journal of Molecular Liquids*, 361:119151, 2022.

[31] Nick Termini, Tony Birri, Brett Smith, Ryan Chesser, Jacob Numbers, Kevin Garland, Ethan Wilgocki, Craig Gray, and Vanda Glezakou. Fy24 progress report on viscosity and thermal conductivity measurements of nuclear industry relevant chloride salts: An experimental and computational study. Technical report, Oak Ridge National Laboratory (ORNL), Oak Ridge, TN (United States), 2024.

[32] Anthony Birri, Nick Termini, Ryan Chesser, Shane Henderson, Jacon Numbers, Ethan Wilgocki, and N. Dianne Bull Ezell. An overview of the molten salt thermal properties database–thermophysical, version 3.1 (mstdb-tp v.3.1). Technical report, Oak Ridge National Laboratory (ORNL), Oak Ridge, TN (United States), 2024.

[33] Jake W Mcmurray, Kaitlin Johnson, Can Agca, Benjamin R Betzler, Dave J Kropaczek, Theodore M Besmann, David Andersson, and N Ezell. Roadmap for thermal property measurements of Molten Salt Reactor systems. Technical report, Oak Ridge National Lab.(ORNL), Oak Ridge, TN (United States), 2021.

[34] SI Cohen and TN Jones. A summary of density measurements on molten fluoride mixtures and a correlation for predicting densities of fluoride mixtures. Technical report, Oak Ridge National Lab.(ORNL), Oak Ridge, TN (United States), 1954.

[35] WD Powers, SI Cohen, and ND Greene. Physical properties of molten reactor fuels and coolants. *Nuclear science and engineering*, 17(2):200–211, 1963.

[36] Stanley Cantor. Density and viscosity of several molten fluoride mixtures. Technical report, Oak Ridge National Lab.(ORNL), Oak Ridge, TN (United States), 1973.

[37] BC Blanke, KW Foster, LV Jones, KC Jordan, RW Joyner, and EL Murphy. Viscosity of fused mixtures of sodium fluoride, beryllium fluoride, and uranium fluoride. Technical report, Mound Plant (MOUND), Miamisburg, OH (United States), 1956.

[38] BC Blanke, EN Bousquet, ML Curtis, and EL Murphy. Density and viscosity of fused mixtures of lithium, beryllium, and uranium fluorides. Technical report, Mound Plant (MOUND), Miamisburg, OH (United States), 1956.

[39] M.W. Rosenthal, R.B. Briggs, and P.R. Kasten. Molten-Salt Reactor Program Semiannual Progress Report For Period Ending Aug. 31, 1968. Technical report, Oak Ridge National Lab.(ORNL), Oak Ridge, TN (United States), 1969.

[40] KO Bobrova, VN Dokutovich, and PN Mushnikov. Thermophysical properties of several molten mixtures of the LiF–BeF2–UF4 system. *Russian Metallurgy (Metally)*, 2023(2):126–135, 2023.

[41] V Khokhlov, I Korzun, V Dokutovich, and E Filatov. Heat capacity and thermal conductivity of molten ternary lithium, sodium, potassium, and zirconium fluorides mixtures. *Journal of nuclear materials*, 410(1-3):32–38, 2011.

[42] A Rudenko, A Redkin, P Mushnikov, E Ilína, S Pershina, O Tkacheva, Yu Zaikov, and S Kumkov. Thermal properties of some molten mixtures in system (naf-kf) eut–uf4. *International Journal of Thermophysics*, 45(8):114, 2024.

[43] Anthony Birri, Nick Termini, Ryan Chesser, and Shane Henderson. An overview of the molten salt thermal properties database–thermophysical, version 4.0 (mstdb-tp v.4.0). Technical report, Oak Ridge National Laboratory (ORNL), Oak Ridge, TN (United States), 2025.

[44] Masamitsu Wakao, K Minami, and Akira Nagashima. Viscosity measurements of molten licl in the temperature range 886–1275 k. *International journal of thermophysics*, 12(2):223–230, 1991.

[45] JW Cooke. Development of the variable-gap technique for measuring the thermal conductivity of fluoride salt mixtures. Technical report, OAK RIDGE NATIONAL LAB., TENN., 1973.

[46] Michael Heinrich Rausch, Kamil Krzeminski, Alfred Leipertz, and Andreas Paul Fröba. A new guarded parallel-plate instrument for the measurement of the thermal conductivity of fluids and solids. *International Journal of Heat and Mass Transfer*, 58(1):610–618, 2013. ISSN 0017-9310. doi: https://doi.org/10.1016/j.ijheatmasstransfer.2012.11.069. URL https://www.sciencedirect.com/science/article/pii/S0017931012009325.

[47] R Mostert, HR Van den Berg, and PS Van Der Gulik. A guarded parallel-plate instrument for measuring the thermal conductivity of fluids in the critical region. *Review of scientific instruments*, 60 (11):3466–3474, 1989.

[48] Moshe Gitterman. Hydrodynamics of fluids near a critical point. *Reviews of Modern Physics*, 50(1): 85, 1978.

[49] SI Cohen and TN Jones. Viscosity measurements on molten fluoride mixtures. Technical report, Oak Ridge National Lab.(ORNL), Oak Ridge, TN (United States), 1957.

[50] Jaewoo Park, Amanda Leong, and Jinsuo Zhang. Density measurements of molten salts. *Journal of Chemical & Engineering Data*, 68(8):1892–1898, 2023. doi: 10.1021/acs.jced.3c00171. URL https://doi.org/10.1021/acs.jced.3c00171.

[51] Brian Merritt, Michael Seneca, Ben Wright, Noah Cahill, Noah Petersen, Austin Fleming, and Troy Munro. Thermal conductivity characterization of fluoride and chloride molten salts using a modified transient hot-wire needle probe. *International Journal of Thermophysics*, 43(10):149, 2022.

[52] Sean G Robertson, Ralph Wiser, Wonseok Yang, Dokyu Kang, Sungyeol Choi, Emilio Baglietto, and Michael P Short. The curious temperature dependence of fluoride molten salt thermal conductivity. *Journal of Applied Physics*, 131(22), 2022.